Soft Matter

PAPER

View Article Online
View Journal | View Issue

Cite this: *Soft Matter*, 2025, **21**, 8300

Evaluating the impact of simulated microgravity of a random positioning machine on the stability of emulsions applying scaling analysis *via* dimensionless numbers

Svenja Schmidt, *[abcd] Modupe N. Adebowale, [ace] Evgeny Rebrov, [f] Ian Fisk, [bdg] Ni Yang, [d] Maria Saarela [hi] and Volker Hessel *[abc]

Random positioning machines (RPM) are commonly used to simulate microgravity for plant growth and cell culturing experiments, but not properly in multi-phase flow studies, *e.g.*, emulsions. The implications of fluid motion induced by RPM movement patterns have only been studied for one-phase system using computational fluid dynamics (CFD). This study investigates the impact of fluid motion of 5 different RPM motion modes (0 g, 0.4 g, clinostat of different frame rates) on dispersed droplets (d_{32} = 0.1–70 μm) applying scaling analysis. These computations are based on well-established fluid-dynamic laws and correlations, thereby giving microgravity researchers easier tool to evaluate potential deficiencies in their study design compared to CFD. We found that the clinostat modes (80 deg s^{-1}; 100 deg s^{-1}; 120 deg s^{-1}) induce a transitional flow regime in the continuous phase, and considerate shear rates acting on the dispersed droplets. Under certain conditions, the shear rates might even impact the average particle size, representing a major corruption in study design, which must not be mistaken as an effect of simulated microgravity. On the other hand, the 0 g and 0.4 g motion modes lead to a laminar flow in the continuous phase, low shear forces, Stokes flow surrounding the dispersed droplets, little relative droplet movement, as well as neglectable forced convection and gravitational force, thus resembling a state similar to true microgravity (0 g motion mode) and partial gravity (0.4 g motion mode).

Received 29th April 2025,
Accepted 5th October 2025

DOI: 10.1039/d5sm00436e

rsc.li/soft-matter-journal

1. Introduction

Emulsions are a popular and practical formulation technique for combining hydrophobic and hydrophilic components in one system. One component is dispersed in the other, and the resulting droplets are stabilized using a surface-active emulsifier. Emulsions are applied in drug delivery and pharmaceuticals[1] to foods[2–4] and cosmetics,[5] while they are also interesting as a reaction environment for the synthesis of chemicals and materials.[6] Due to their widespread use, emulsions are attractive for in-space manufacturing, *i.e.*, the on-demand manufacturing in space to facilitate long-term space exploration. Products and materials that are required during long-term space missions are produced from bulk materials, space resources and space-grown plants as they are needed, therefore saving valuable storage room on space shuttles.[7] Emulsions have the potential, for example, to advance personalised health care in space. Personalised health care describes a recent approach in medicine that argues for monitoring individual health data, environmental factors, lifestyle, and genetics to prevent disease as well as manage disease more efficiently instead of the current-day practise of impersonal care of acute disease.[8] During the in-space manufacturing of medicine and functional foods, their formulation could be adjusted based on individual exposure data from health monitoring sensors. For instance, our laboratory is developing a beverage system[9] that enables personalisation of the beverage's formulation by adjusting nutrient content while providing a choice in flavours.

[a] *School of Chemical Engineering, Adelaide University, Adelaide 5005, Australia. E-mail: svenja.schmidt@adelaide.edu.au, volker.hessel@adelaide.edu.au*
[b] *ARC Centre of Excellence in Plants for Space, Adelaide University, Waite Campus, Urrbrae 5064, Australia*
[c] *Andy Thomas Centre for Space Resources, Adelaide University, Waite Campus, Urrbrae 5064, Australia*
[d] *International Flavour Research Centre, University of Nottingham, Sutton Bonington Campus, Loughborough LE12 5RD, UK. E-mail: svenja.schmidt@nottingham.ac.uk*
[e] *School of Pharmacy, University of Nottingham, University Park, Nottingham NG7 2RD, UK*
[f] *School of Engineering, University of Warwick, Coventry CV4 7AL, UK*
[g] *International Flavour Research Centre (Adelaide), Adelaide University, Waite Campus, Urrbrae 5064, Australia*
[h] *South Australian Research and Development Institute, School of Agriculture (SARDI), Adelaide 5001, Australia*
[i] *School of Agriculture, Food, and Wine, Adelaide University, Waite Campus, Urrbrae 5064, Australia*

As space is a vastly different environment to Earth, it is critical to understand the influence of the local conditions on the respective manufacturing endeavour. In case of emulsions, space conditions can not only influence the in-space emulsification but also impact the long-term stability of emulsions, including emulsion-based products taken-along from Earth. Considerable space conditions are the significant increase in cosmic radiation due to being outside the Earth's protective atmosphere and the significant reduction in gravitational forces leading to a perceived weightlessness. In this study particularly, we are focusing on the impact of microgravity on emulsion stability.

Emulsions are thermodynamically unstable systems, *i.e.*, both phases will eventually separate over time, and different mechanisms contribute to emulsion separation. Apart from leaking droplets, the main driver in emulsion instability on Earth is gravity: the density difference between the dispersed phase and continuous phase leads to sinking (sedimentation) or rising (creaming) of the dispersed phase, and therefore phase separation. Droplet–droplet interactions like flocculation, coalescence, and Ostwald ripening may enhance the effect of creaming and sedimentation.[10] As the main driver of emulsion instability is absent in space, emulsion instability is mainly driven by diffusion,[11] potentially leading to a considerably different outcome in emulsion evolution.

However, studying the impact of microgravity is difficult as the access to in-space laboratory space on the ISS is highly limited and associated with considerable costs. Researchers typically resort to alternative experimental setups on Earth (parabolic flight, drop tower, benchtop lab-devices) and in low earth orbit (LEO; sounding rockets, satellites), see illustration in the SI. While sounding rockets and satellites allow to conduct experiments in space, studies require considerable preparation and potentially an automated experimental setup, as both are lacking the option of crewed missions. For microgravity studies on Earth, parabolic flights and drop towers can only simulate microgravity for a few seconds, as they are limited by how long an object is exposed to a free fall. For example, ESA's main drop tower, operated by ZARM and located at the University of Bremen, provides a free fall of 120 m leading to 4.74 s of microgravity.[12] Both the parabolic flight and the drop tower also come with the limitation of hypergravity ($g > 1$) present during deceleration (*e.g.*, 50 g for drop tower[12]). Benchtop devices such as the clinostat (2D and 3D) and the random positioning machine avoid exposure to hypergravity, are the easiest to access, and offer long-term exposure to simulated microgravity. A 2D-clinostat device consists of a horizontally positioned mount, which exposes a sample to a rotation in vertical direction to the gravitational vector (consistent movement *via* rotation around 1 axis). In comparison, both the 3D-clinostat and the RPM have a more complex setup: two frames are interconnected in a way which enables rotation in all directions. While the 3D-clinostat can randomly vary the rotational speed, RPMs can additionally also change randomly the direction of the rotation.[13] In all cases, the controlled movement is designed to equalise the gravity vector.[14] This type of microgravity simulation cannot simulate some of the unique physical effects present in space, *e.g.*, the Marangoni effect, but *via* consistent movement or acceleration against the downward-facing gravity vector, the gravity vector becomes negligible over extended exposure to these movement pattern. Due to the extended exposure required to reach a mircogravity-like state, this kind of microgravity simulation is only suitable for slow processes taking place over long time scales.[15] For this study, the authors had access to the RPM device designed by Airbus for ESA (RPM 2.0, now managed by Yuri),[16,17] which apart from randomised (speed, direction) 3D-rotation also offers a clinostat motion mode, in which the outer frame is fixed in place, thereby only allowing rotation around one axis. To the author's best knowledge, Airbus' RPM device is the most used, commercially distributed RPM, with one other company providing a similar-sized RPM in Northern America (equiprobe random positioning machine).[18] Otherwise, using a self-designed device for microgravity simulation has been reported, most notably the RPM designed by the polish analog astronaut training center.[19] Other examples involve a dual axis rotating frame machine in combination with appropriate software as RPM, however, these can be restricted in angular excursion.[20] Design approaches *via* 3D printing have been investigated for 3D clinostat devices to obtain systems customised in size.[21,22]

While RPM and clinostat devices are popular for cell[23–25] and plant cultivation,[26–28] the authors could only find one example of a study investigating the impact of simulated microgravity on nanoemulsion stability, with most studies evolving around active and passive soft matter having been conducted in low earth orbit.[29,30] In the study of nanoemulsions exposed to microgravity simulated by a 3D-clinostat (model not mentioned), nanoemulsions remained stable over a time of 7 days.[20] Yet, the study did not discuss the effect that the randomised 3D movement might have on the samples. The extended rotation induces forced convection in fluid samples, *i.e.*, a fluid motion that is caused by an external source. In this regard, simulated microgravity differs vastly from true microgravity in space. Depending on the effect of the fluid motion on the samples, the simulation of microgravity could be considerably corrupted. The induced fluid flow might even impact the characteristics of the samples studied (*e.g.*, change in average droplet size in emulsions), which could be misidentified as an effect of microgravity. Not addressing the effects of fluid dynamics in simulated microgravity experiments can therefore lead to a major misinterpretation of experimental findings.

To the authors' best knowledge, there are only two studies investigating specifically the fluid-dynamics of vessels filled with liquids on an RPM,[31,32] yet only one-phase systems are considered. Both studies find that a considerable flow motion occurs during RPM experiments, which needs to be taken into consideration in experimental design to avoid a depletion of the simulated microgravitational effect. In both studies, flow simulations based on a mathematical model solved *via* numerical methods are applied to predict the behaviour of the fluid, otherwise called computational fluid dynamics (CFD).

While CFD offers the to-date most accurate way of predicting fluid flow (given appropriate assumptions and boundary conditions), it requires profound understanding about continuity and momentum relations, typically *via* solving the Navier Stokes equation, as well as advanced knowledge of applying numerical methods. This makes CFD less accessible for researcher of other backgrounds and prevents scientists to incorporate fluid-flow considerations in their study design on simulated microgravity. As alternative to CFD, the authors suggest applying scaling analysis, *e.g.*, reported correlations, force balances, and dimensionless numbers, for fluid flow estimation, particularly for systems with a dispersed phase (*e.g.*, droplets, particles, cells/bacteria). While giving no information about the flow differences inside the experimental vessel, it allows for a quick evaluation of the state of flow in the continuous phase averaged over the whole experimental vessel as well as the fluid flow surrounding the dispersed phase. Scaling analysis *via* dimensionless numbers have been used to describe nanoemulsion formation *via* high pressure homogenization and ultrasonication.[33] The methods proposed could serve as an easier tool for researchers of all backgrounds to estimate whether the forced convection induced by the RPM has an impact on their dispersed phase, and if necessary, adjust the movement settings to achieve the desired effect. While this study focuses on Airbus' RPM, the methods proposed are suitable to be transferrable to other microgravity simulations, given the devices offer a way to record their movements over time as location coordinates.

In summary, it is essential to know the true influence of microgravity in the respective systems to accelerate the development of new in-space manufacturing technologies. To be able to use alternatives to costly and difficult-to-access studies in space, their limitations in simulating microgravity needs to be considered in order to avoid corrupting experimental findings. Therefore, the aim of this study is (i) to assess the methods of scaling analysis *via* dimensionless numbers for the fluid flow in the experimental vessel and (ii) to evaluate the effect of microgravity and partial gravity simulated by an RPM in different motion modes on emulsions, while focusing particularly on the following questions:

- What is the fluid flow regime in the continuous phase?
- Can the shear forces induced by forced convection impact the average droplet size of the dispersed phase?
- How do the droplets move relatively to the movement of the continuous phase?
- Can the RPM generate a state of simulated microgravity comparable to true microgravity?

2. Methods

2.1. Overview of symbols, notations, and dimensionless numbers

Tables 1 lists all symbols and notations used in the following, while Table 2 gives a short explanation of the relevant dimensionless numbers.

2.2. Random positioning machine

2.2.1. Layout of the random positioning machine. The random positioning machine (RPM 2.0, Airbus Netherlands B.V., Leiden, the Netherlands, nowadays distributed by Yuri GmbH, Meckenbeuren, Germany) is a benchtop device (footprint: 38 × 31 × 35 cm^3, weight: 7.5 kg[17]) to simulate microgravity (0 g) and partial gravity (0 g < partial gravity < 1 g) under terrestrial gravity conditions *via* 3D and 2D movement (space in *x*-, *y*-, *z*-direction and plane in *y*-, *z*-direction, respectively, in Fig. 1(b)). The operational principle is to equalize the vector of the terrestrial gravitation (defined as acceleration, unit m s^{-2}) over time by random movement (speed and/or direction, applied for microgravity or partial gravity motion modes, see next section and SI) or alternatively, achieve a state of extended free fall *via* constant rotation (speed and direction, applied for clinostat motion mode, see next section and SI). The 3D movement is achieved *via* two interconnected frames (see Fig. 1(a) and (b)). The outer frame, which is mounted to the stand, can rotate horizontally (around the *z*-axis, see Fig. 1(b)) while the inner frame, which is connected to the outer frame, can rotate vertically to the position of the outer frame. With the outer frame fixed in place, the inner frame rotates only around the *x*-axis (clinostat motion mode, see Fig. 1(b)). Combining the movement of both frames simultaneously enables a movement in all 3 dimensions (*x*-, *y*-, and *z*-axis in Fig. 1(b)). The inner frame provides 5 fixtures (see Fig. 1(c)) to install the experimental platform to. The experimental platform serves as a mount for experimental setups (up to 1.5 kg and smaller than 15 × 15 × 15 cm^3;[17] *e.g.*, agar plates, greenhouses, vials). Changing the position of the experimental platform *via* the fixtures allows to change the distance to the centre of rotation, *i.e.*, the radius of platform's rotation $r_{rotation}$ (2.3–7.5 cm in 1.3 cm increments).

2.2.2. Modes of operation of the random positioning machine. The RPM offers different movement options for the frames in its accompanying software, so-called motion modes (for a detailed overview see Table S1 in SI). Apart from motion modes which provide random 3D movement (random direction and speed) and constant 3D movement (random direction, constant speed), there are motion modes to simulate microgravity (0 g) and partial gravity (0.1–0.9 g in 0.1 g increments, lunar gravity, Martian gravity). For these motion modes, the frames will follow a predefined motion path (3D movement) to constantly change the position of the experimental vessel relative to the gravitational vector. The motion path also predefined the frame speed of both the inner and outer frame at any time, with the frame speeds changing constantly (max. frame speed: 15 deg s^{-1}, see also SI). Both the control of speed and position of the experimental vessels allows to average the gravity vector to the anticipated values. The predefined motion path is automatically looped to obtain the desired experiment duration. Additionally, there is a clinostat setting, which aims to simulate microgravity by circular 2D movement. With the outer frame fixed horizontally in place, the experimental platform rotates at constant speeds around the *x*-axis (see Fig. 1(b)), moving the experimental

Table 1 List of symbols and notations; items are listed in order of appearance

Symbols and notations	Description	Unit
g	Gravity	m s^{-2}
g_{Earth}	Terrestrial gravity	m s^{-2}
g_{Mars}	Martian gravity	m s^{-2}
g_{moon}	Lunar gravity	m s^{-2}
$r_{rotation}$	Radius of the rotation of the experimental platform of the random positioning machine (RPM)	m
x; y; z	Location coordinates, output the RPM	—
Δt; t; t_0	Time interval location coordinates are recorded; time; start time of the RPM	s
g_t	Simulated gravity at time t	g
$x_{average,t}$; $y_{average,t}$; $z_{average,t}$	Averaged location coordinates at time t	—
n_t; n_t^*	Number of location coordinates recording; number of location coordinates recording excluding ramp-up phase	—
$g_{average}$	Simulated microgravity averaged over runtime excluding ramp-up phase	g
g_r'	Simulated microgravity at radius r to the centre of rotation	g
ω	Frame speed of the RPM	rad s^{-1}
SOR	Surfactant-to-oil ratio	—
$m_{surfactant}$	Mass of surfactant present in oil phase	g
m_{oil}	Mass of oil present in oil phase	g
$\rightarrow$	Indicates a vector	n/a
Droplet	Parameter defined for dispersed droplets	n/a
cont	Parameter defined for the continuous phase	n/a
F_B	Buoyancy	N
F_G	Gravitational force	N
F_D	Drag force	N
$w_{d,rest}$	Stationary relative particle velocity for a resting system	m s^{-1}
r	Radius	m
ρ	Density	kg m^{-3}
F_d	Stokes' drag	N
μ	Dynamic viscosity	Pa s
A; B	RPM platform moves from point A to point B within Δt	—
a_1; a_2; a_3; b_1; b_2; b_3	Location coordinates for point A and point B	m
$\lvert\overrightarrow{AB}\rvert$	Connecting vector of point A and point B	m
α	Angle between point A and point B to the centre of the inner frame	°
L	Circular arc L between point A and point B	m
$v_{A\rightarrow B}$	Platform velocity between point A and point B	m s^{-1}
w_{cont}	Velocity of the continuous phase	m s^{-1}
$w_{cont,average}$	Velocity of the continuous phase averaged over RPM runtime excluding ramp-up phase	m s^{-1}
Re_{cont}	Reynolds number of the continuous phase	—
h	Characteristic length of geometry	m
d_{hyd}	Hydraulic diameter	m
A_{duct}	Cross-sectional area of a duct	m^2
U_{duct}	Wetted perimeter of the cross-section of a duct	m
ΔW_{shear}	Work induced by the shear forces acting on the droplet	J
ΔG_{Form}	Free energy of emulsion formation	J
F_S	Shear force	Pa
$\dot{\gamma}$	Shear rate	s^{-1}
$A_{droplet}$	Cross-sectional area of the droplet	m^2
ΔW	Change in free energy of the interface	J
ΔS	Change of entropy in the system	J K^{-1}
σ	Interfacial tension	N m^{-1}
$\Delta A_{surface}$	Change in surface area of the droplets induced by emulsification	m^2
Bo	Bond number	—
ζ	Drag coefficient	—
$w_{d,conv}$	Stationary relative particle velocity for a system with forced convection	m s^{-1}
$w_{d,abs}$	Absolute droplet velocity	m s^{-1}
Re_p	Reynolds number for particles	—
$Re_{p,solid}$	Reynolds number for solid particles	—
Ar	Archimedes number	—
ν	Kinematic viscosity	m^2 s^{-1}
$Re_{p,liquid}$	Reynolds number for liquid particles	—
Ri	Richardson number	—
Gr	Grashof number	—
β	Linear expansion coefficient	$°C^{-1}$
T	Temperature	°C

vessel on an yz-plane. In this case, the frame speed is not predefined but is set in the control software by the user (max. frame speed: 120 deg s^{-1}, see also SI). For accurate microgravity simulation in clinostat motion mode, it is mandatory to position the outer frame horizontally prior to starting the RPM.

Table 2 List of dimensionless numbers

Symbol	Name	Description	Characteristic values
Re_{cont}	Reynolds number (continuous phase)	Ratio of inertial forces to viscous forces in the continuous phase	Pipe and duct geometry: $Re_{cont} < 2300$: laminar flow; $2300 < Re_{cont} < 4000$: transition region; $Re_{cont} > 4000$: turbulent flow;
Re_p	Reynolds number for particles	Ratio of inertial forces to viscous forces around the particle	$Re_p < 0.1$: Stokes flow; $0.1 < Re_p < 20$: flow streamlines lose symmetry; $Re_p > 20$: flow streamlines detach;
Bo	Bond number	Ratio of the gravitational forces to the surface forces	Bo < 1: surface forces dominate; Bo > 1: gravitational forces dominate;
Gr	Grashof number	Ratio of buoyancy to viscous forces	Gr < 1: viscous forces dominate; Gr > 1: buoyancy dominates;
Ri	Richardson number	Ratio of natural convection to forced convection	Ri < 10: forced convection dominates; Ri > 10: natural convection dominates;

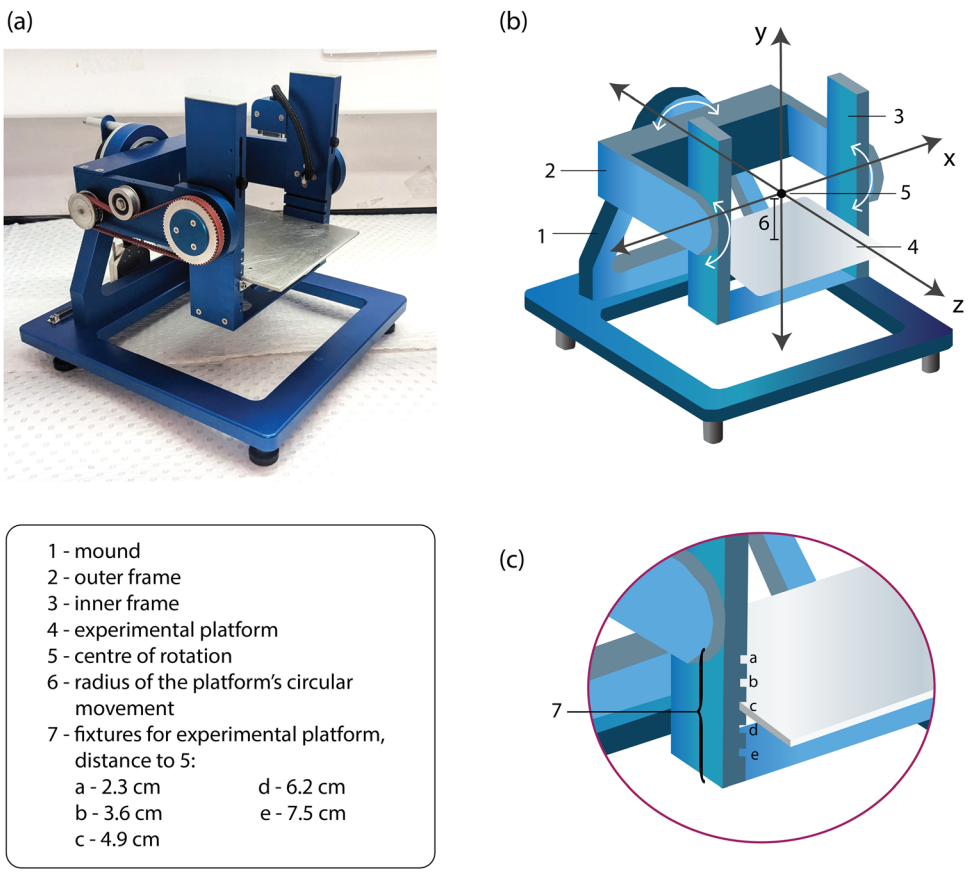

Fig. 1 Layout of the random positioning machine (RPM): (a): picture of the RPM 2.0 obtained from Airbus; (b) illustration of the RPM showing major parts and geometry; (c) close-up of fixtures for the experimental platform.

This study focuses on the 0 g and clinostat motion mode (frame speeds: 80 deg s^{-1}, 100 deg s^{-1}, 120 deg s^{-1}) to simulate microgravity and the 0.4 g motion mode to simulate partial gravity. The 0 g motion mode was chosen as it is the standard approach to simulate microgravity with the RPM 2.0 at a set range of low frame rates (max. 15 deg s^{-1}), while the clinostat motion mode allows to set higher frame speeds for a microgravity simulation (max. 120 deg s^{-1}). 0.4 g motion mode was chosen as an example for a partial gravity simulation close the Mars gravity (0.39 g), which operates at the same frame rates as the 0 g motion mode (max. 15 deg s^{-1}).

2.2.3. Determining the simulated microgravity and partial gravity based on RPM movement data. The RPM gives the option to record the movement of the platform over the duration of the experiment. For this study, dimensionless location coordinates for x, y, and z were recorded every approx. 1.1 s (= Δt) over the course of 24 h using the 0 g motion mode (microgravity), 0.4 g motion mode (partial gravity), and the clinostat motion mode at frame speeds of 80 deg s^{-1},

100 deg s^{-1}, and 120 deg s^{-1}. At the start time t_0, of the RPM the gravity is 1 g, *i.e.*, terrestrial gravity. As the RPM starts moving, the gravity decreases gradually until it reaches the intended gravity values (ramp-up phase). Averaging the location coordinates (eqn (1)), allows to calculate the simulated gravity g_t at time t (unit: g) after t_0 of the RPM[34] (eqn (2)).

$$x_{\text{average},t} = \frac{1}{n_t}\sum_{i=1}^{n_t} x \tag{1}$$

$$g_t = \sqrt{x_{\text{average},t}{}^2 + y_{\text{average},t}{}^2 + z_{\text{average},t}{}^2} \tag{2}$$

As the RPM changes velocities consistently over the run time to average the terrestrial gravity, the values for the simulated gravity change slightly between different time points. The average simulated gravity g_{average} was obtained by calculating the average of g_t over the run of the RPM, excluding the initial ramp-up phase. For this study, the ramp-up phase was assumed to be one hour for all motion modes.

$$g_{\text{average}} = \frac{1}{n_t^*}\sum_{i=1^*}^{n_t^*} g_t \tag{3}$$

The average simulated gravity g_{average} is only valid at the centre of the rotation ($r_{\text{rotation}} = 0$) at indefinitely small dimensions of the experimental vessel. However, this does not reflect realistic experimental conditions. Depending on the experimental vessel and the equipment used, a positioning in the centre of the rotation is not possible, or experimental vessel dimensions exceed largely the centre of the rotation. Eqn (4) estimates the average simulated gravity at radius r to the centre of the rotation g'_r.[35]

$$g'_r = \frac{\omega^2 r}{g_{\text{Earth}}} \tag{4}$$

2.3. Emulsion data used for fluid-dynamic characterisation

2.3.1. Emulsification principle for model emulsions. To investigate the impact of the RPM's movement on dispersed droplets in an emulsion, it is advisable to consider a range of droplet sizes from nanoemulsions (diameter $<$ 200 nm) to conventional emulsions (diameter $>$ 200 nm). We decided that a data set of a model emulsion system with particle sizes ranging from 100 nm to 70 μm, which was obtained during an earlier study,[9] was best suited. The emulsions were generated using a new emulsification method, *i.e.*, the combination of a solvent-free variant of the spontaneous emulsification with a microfluidic process. The spontaneous emulsification is a low-energy emulsification method, which facilitates self-assembly of droplets *via* physicochemical properties of the emulsion components involved. In this case, the surfactant polysorbate 80 was employed which can be dissolved both in oil and water, but has a higher hydrophilicity as indicated by its hydrophilic-lipophilic balance (HLB) of 15.[36] When initially dissolved in the oil, polysorbate 80 diffuses rapidly into the aqueous phase upon the formation of an interfacial area, forming small droplets in the process,[37–39] see Fig. 2(a). In the following, the term oil phase is defined as a lipophilic phase containing the oil medium-chain triglycerides and polysorbate 80. The spontaneous emulsification is significantly influenced by surfactant concentration, often characterised in the form of surfactant-to-oil ratio considering the masses of both components of the oil phase.[40]

$$\text{SOR} = \frac{m_{\text{surfactant}}}{m_{\text{oil}}} \tag{5}$$

Microfluidics is a term for a type of continuous chemical reactors, in which all fluid channels have a diameter below approx. 1 mm. This allows for precise fluid control (flow, temperature) under unique physical conditions (laminar flow prevails, strong capillary forces, enhanced mass transport).[41–43] In this case, a single-contact microfluidic mixer of simple geometry, *i.e.*, a tee connection (or T-mixer) was used. The T-mixer fed the oil phase into the aqueous phase, so that initial droplets would be formed *via* shear forces caused by the current of the aqueous phase, with the initial droplets then disintegrating into many smaller, secondary droplets *via* the spontaneous emulsification,[9] see Fig. 2(b).

2.3.2. Production of beverage emulsions. The oil phase consists of varying ratios (SOR: 0.05–1.5) of medium-chain triglycerides (pharmaceutical grade, Vials Direct, Salamander Bay, NSW, Australia) as oil and polysorbate 80 (Tween® 80, Sigma-Aldrich Truganina, VIC, Australia) as surfactant. To prepare the oil phase of the respective SOR, oil and surfactant at the required mass were stirred at 600 rpm (RCT Basic magnetic stirrer, IKA®, Staufen, Germany) for 30 min at room temperature. The aqueous phase consists of 5 mM phosphate buffer (1 M stock solution from Sigma-Aldrich Truganina, VIC, Australia; diluted with Milli-Q water). For the continuous emulsification, the oil phase was placed at the inlet of pump A, while the aqueous phase was placed at the inlet of pump B (both Azura P4.1S 10 ml Knauer, Berlin, Germany). In case of high viscosities (working limit of pumps: 100 mPa s), the oil phase was heated to approx. 40 °C while stirred at 400 rpm, and a heating mat (seedling heat mat, 10″ × 20.75″, T_{max} = 42 °C) was placed around the inlet and pump A to elevate the temperature in the immediate surrounding. A T-mixer with an internal diameter of 0.5 mm (Tee LP PEEK 1/4–28 1/16″ 0.040″, Upchurch Scientific®, IDEX Health & Science, Lake Forest, USA) was connected *via* transparent tubing (internal diameter 1 mm, 1/16″ OD, 0.040″ ID) to the outlet of the pumps (see Fig. 2(b) for accurate setup). The outlet of the T-mixer led *via* tubing to a beaker, which collected the formed emulsion. Prior to experimentation, pump A was purged with ethanol to reduce the risk of jellification of the oil phase at low water concentrations which can lead to blockages and equipment damage. After starting the pumps (volumetric flows were determined to obtain concentrated emulsion with 10 wt% oil, for volumetric flows and their determination see Section S2 in SI), emulsion generated within the initial 7 min was discarded to

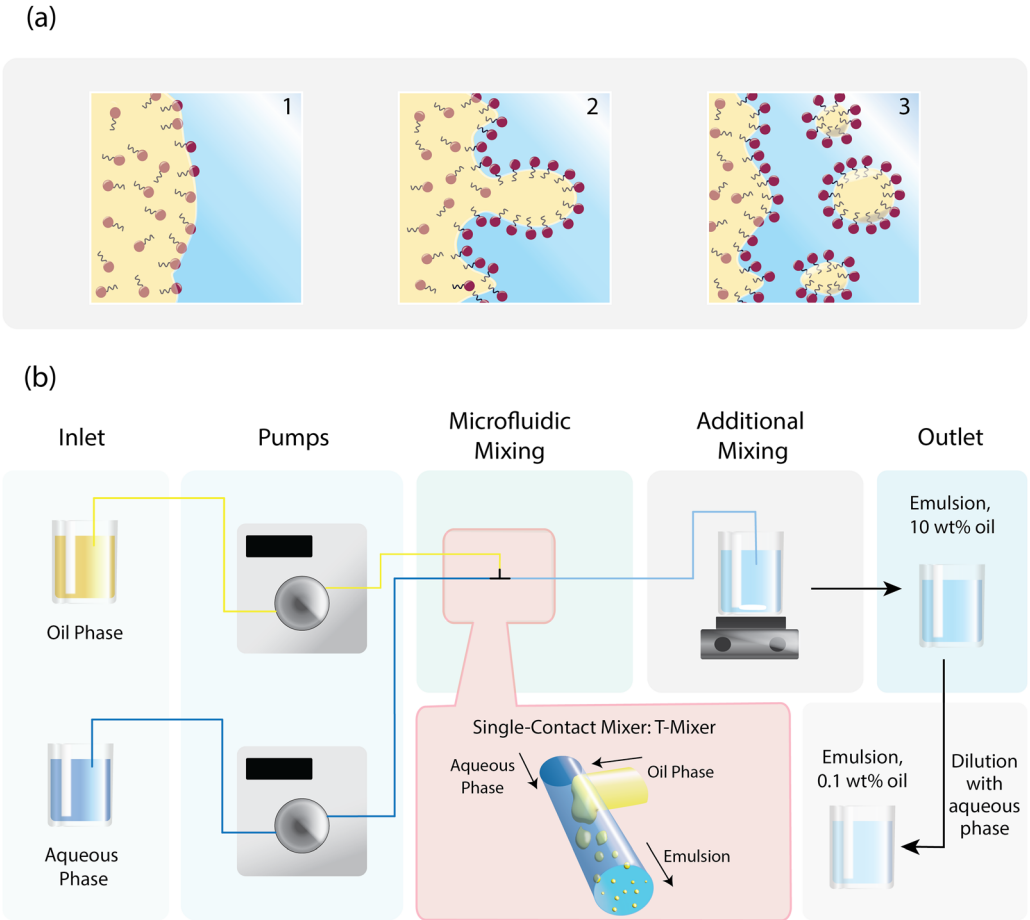

Fig. 2 (a) Visualisation of the spontaneous emulsification: 1 – oil and aqueous phase come into contact, 2 – deformation of interface, 3 – diffusion of surfactant into the aqueous phase with simultaneous droplet formation; (b) visualisation of the experimental setup.

allow the system to reach equilibrium conditions. Then, emulsion was collected for 5 min at the outlet while being stirred at 600 rpm. After sample collection, the emulsion was stirred for 10 min, which allowed thorough combination of both phases. To obtain beverage emulsions (0.1 wt%), the concentrated emulsion was diluted manually with phosphate buffer (5 mM).

2.3.3. Characterisation of the surfactant, oil, oil phase and beverage emulsions. To characterise the surfactant, oil, and oil phase, density and dynamic viscosity were determined. For the oil phase, these characteristics were determined in relation to the SOR (0.05–1.5). For density, 10 mL of oil or respective oil phase were drawn up from bulk into a syringe (size: 10 mL, luer slip, concentric tip, Terumo®, Laguna, Philippines) and weighted with a precision balance (PRseries, Ohaus®, New Jersey, USA) in a temperature-controlled room (room temperature: 22–24 °C). In the case of a mixing gap (SOR < 0.5), the oil phase was stirred during sample collection. The measurement was repeated at least 10 times, and the average density was determined.

For dynamic viscosity, a sample of the surfactant, oil, or oil phase given on the plate fixture of a rotational rheometer (cone and plate fixture, 20 mm, Universal Stress Rheometer SR5, Rheometric Scientific™). The temperature was set to 20 °C *via* a temperature controller (Universal Stress Rheometer SR5 Enviromental System, Rheometric Scientific™) connected to a water circulator (F25, Julabo GmbH, Seelbach, Germany). A dynamic frequency sweep test (shear rate range: 0.01–10 s^{-1}) was performed. As in all cases, the relation between shear stress and shear rate was linear, it was concluded that the oil phase and its constituents were Newtonian fluids, and their viscosity was determined as slope of the shear stress in relation to the shear rate. The measurement was repeated 4 times, and the average viscosity was determined. Due to the mixing gap below SOR of 0.5, dynamic viscosities were determined *via* linear regression of experimentally determined oil phases of SOR 0.5–2.0 with pure medium-chain triglycerides oil set as *y*-intercept.

To characterise the beverage emulsion, the particle size d_{32} (Sauter diameter) was determined in relation to the oil phases' SOR. Measurement was done immediately after emulsification to reduce effects of potential, time-dependant instability mechanisms using a static light scattering instrument (Mastersizer 2000 with a Hydro 2000MU Unit, Malvern Instruments Ltd, Malvern, UK). Concentrated emulsion was slowly added into the wet sample dispersion unit (filled with 5 mM phosphate buffer, stirred at 750 rpm) until a suitable turbidity is reached. The refractive index of medium-chain triglycerides

was set to 1.445.[40] Each measurement determined particle size in triplicate and particle size measurement was repeated 3 times for each emulsion. The average particle size was determined.

2.3.4. Characteristics of the oil, surfactant, oil phase and the beverage emulsions. The medium-chain triglyceride oil stems from coconut oil, which has been fractioned to obtain medium-chain triglycerides[44] (triglycerides containing 2–3 medium-chain fatty acids, in this case mainly capric and caprylic fatty acids; density ρ at RT: 953.9 kg m^{-3}; kinetic viscosity μ at 20 °C: 31.7 mPa s). Polysorbate 80 (systematic name: polyoxyethylene (20) sorbitan monooleate, formula: $C_{64}H_{124}O_{26}$; molar mass M as provided from the manufacturer: 1310 g mol^{-1}; density ρ at RT as provided from the manufacturer: 1060 kg m^{-3}; kinetic viscosity μ at 20 °C: 727.9 mPa s) is a synthetic, non-ionic surfactant.

Increasing the surfactant content, or SOR, in the oil phase increased both the density and viscosity of the bulk oil phase, see Fig. 3(b) and (d). At the same time, increasing the surfactant content in the oil phase influenced strongly the spontaneous emulsification. Up to an SOR of 0.75, the droplet size decreased with increasing surfactant content. Above an SOR of 0.75, the droplet size remained constant with increasing surfactant content. It is assumed that in this area, the spontaneous emulsification is limited by the emulsification setup: the setup does not allow to further decrease the droplet size with increasing surfactant content, as the smallest droplet size obtainable with a continuous single-contact microfluidic mixer is already reached. Limiting factor might be the size of the initial droplets created *via* the mixer's internal geometry and flow regime. The influence of the surfactant content in the oil phase is also reflected in Fig. 3(c) and (e), which visualize the relation between the average droplet size (*x*-axis) and density (*y*-axis in Fig. 3(c)) and viscosity (*y*-axis in Fig. 3(e)) of the oil phase. For the full data set, please refer to Section S3 in the SI.

2.3.5. Assumptions for subsequent modelling. The following assumptions on the emulsion system have been made for the modelling:

(1) The oil droplets are equally distributed in the aqueous phase.

(2) Due to the low oil content in the emulsion, the distance between single droplets is large enough to avoid particle–particle interactions, including particle swarm behaviour and instability mechanisms such as flocculation and coalescence.

(3) No temperature or concentration gradient is present in the emulsion, otherwise causing natural convection and droplet movement.

(4) The continuous phase and the final emulsion have approximately the same viscosity and density as water (997 kg m^{-3} and 1.002 mPa s, respectively).

(5) Leaking of the surfactant into the aqueous phase is negligible. Instead, it remains mainly at the surface of the droplet or in case of excess surfactant, inside the droplets. Therefore, both the dispersed phase and the continuous phase have the same characteristics (viscosity, density) as the bulk phase.

During exposure for simulated microgravity, it is assumed that emulsions are contained in common sample vials which do not contain air bubbles. Specifically, we considered small-volume vials (7 mL clear screw top vials with polypropylene hole caps with a PTFE/silicone septum, Supelco®, Bellefonte, Pennsylvania, USA). 10 different vials were measured to obtain accurate dimensions (see Fig. 5(c)).

2.4. Overview of the model cases

Three different cases (a)–(c) have been chosen to evaluate the effect of the RPM's different motion modes on emulsion stability, *i.e.*, (a) a resting system in terrestrial gravity, (b) simulated microgravity in terrestrial gravity with the working principle based on forced convection, and (c) true microgravity as observed in space (see Fig. 4).

(a) Resting system in gravity

The first case represents a resting system in gravity, *i.e.*, a system without any external movement and therefore without forced convection. The dispersed droplet is exposed to the buoyancy $\overrightarrow{F_B}$, the gravitational force $\overrightarrow{F_G}$, and the drag force $\overrightarrow{F_D}$. The buoyancy acts in the opposite direction to the gravitational force, which pulls the droplets towards the centre of the respective object with gravitational attraction (typically celestial bodies, *e.g.*, Earth: terrestrial gravity, moon: lunar gravity, and mars: martian gravity). The difference in density between continuous phase and dispersed droplets determines the direction of movement of the droplet: if the droplet's density is higher than the continuous phase's density, gravitational force prevails, and the droplet sinks to the bottom. If the droplet's density is lower than the continuous phase's density, buoyancy prevails, and the droplet rises to the surface. The drag force is directed in the opposite direction of the overall movement of the droplet. In general, when an object moves through a fluid, the drag force is composed of the form drag (= differences in pressure on the front and rear of the object) and the viscous drag (= friction between the fluid and the object's surface). The drag force can be determined by the resulting balance of forces, see eqn (6):

$$\overrightarrow{F_D} = \overrightarrow{F_G} - \overrightarrow{F_B} \quad (6)$$

(b) Simulated microgravity in terrestrial gravity

The second case represents a liquid sample installed on the RPM. The movements of the RPM lead to forced convection in the liquid and induces a liquid flow. In this case, it is assumed that the liquid moves at a constant speed within the time interval Δt, resulting in a stationary particle movement. Since the RPM enables 3D movement, the volume flow can occur in any direction within the vial. Since the RPM is used on Earth, the terrestrial gravitational force $\overrightarrow{F_{G,Earth}}$ pulls the droplet towards the centre of the Earth, while the buoyancy $\overrightarrow{F_{B,Earth}}$ acts in the opposite direction of the terrestrial gravitational force. Again, the difference in densities determines whether buoyancy or gravity dominates. In case of a laminar flow, in which droplet movement is not influenced by turbulences in the continuous phase, droplets can move upward (lower droplet density compared to density of continuous phase) or downward

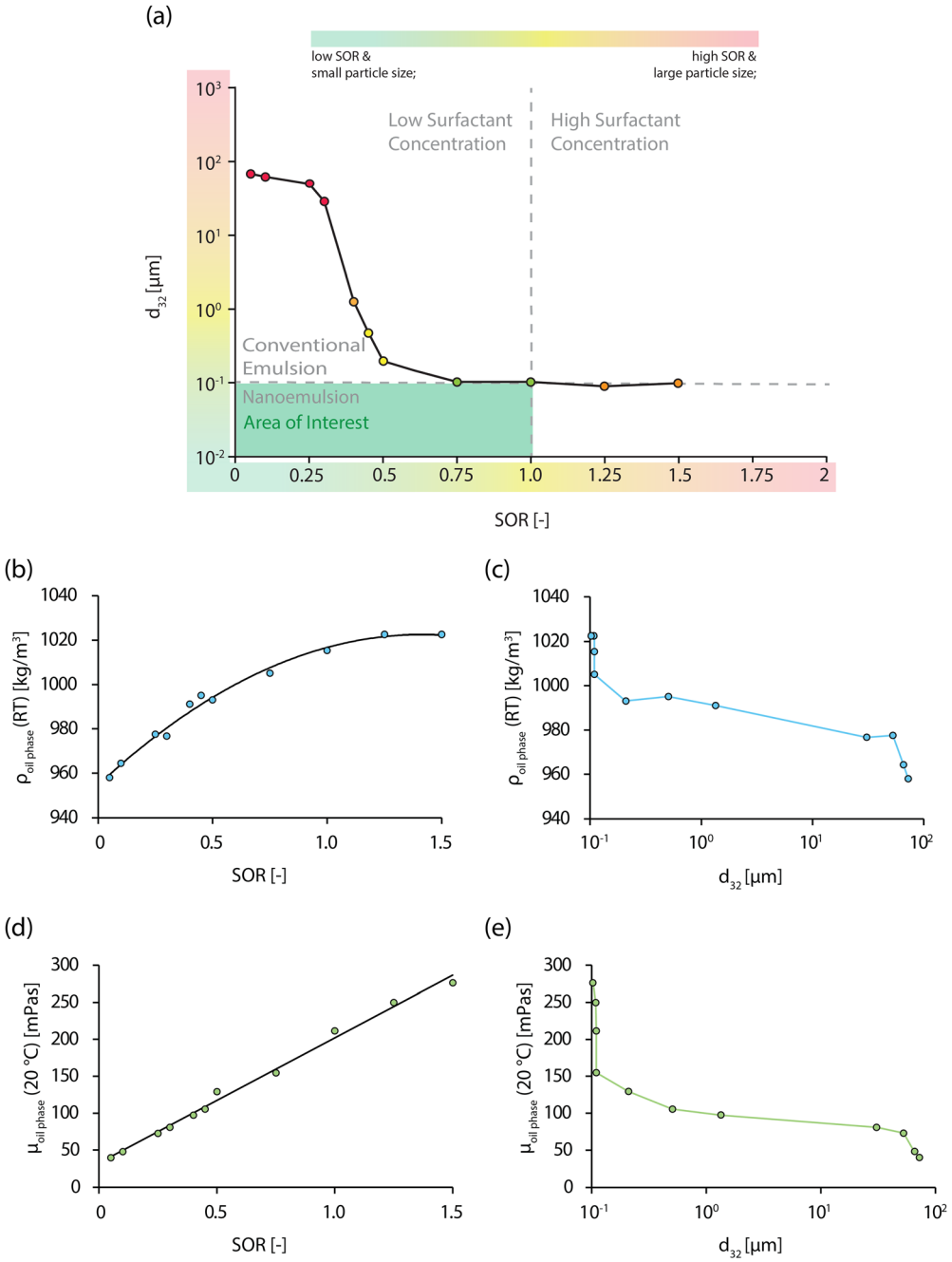

Fig. 3 (a) Average particle size d_{32} in relation to surfactant-to-oil ratio SOR; (b) density of the oil phase $\rho_{\text{oil phase}}$ at room temperature in relation to surfactant-to-oil ratio SOR; (c) density of the oil phase $\rho_{\text{oil phase}}$ in relation to average particle size d_{32}; (d) dynamic viscosity of the oil phase $\mu_{\text{oil phase}}$ at 20 °C in relation to surfactant-to-oil ratio SOR; (e) dynamic viscosity of the oil phase $\mu_{\text{oil phase}}$ at 20 °C in relation to average particle size d_{32}; all emulsions are oil-in-water emulsions (oil phase: mixture of medium-chain triglycerides and polysorbate 80, aqueous phase: phosphate buffer, 5 mM) obtained *via* spontaneous emulsification carried out in a continuous, microfluidic process (T-mixer with internal diameter of 1 mm), adapted from ref. 9.

(higher droplet density compared to density of continuous phase), while carried along by the direction of flow. Droplet separation can be prevented when the flow of the continuous phase is sufficient to counterbalance any dominating gravity or buoyancy. The drag force $\overrightarrow{F_D}$ (result of form drag and viscous drag) acts in opposite direction to the direction of the droplet movement, *i.e.*, the direction of volume flow. Eqn (7) describes the resulting balance of forces, which act on a dispersed droplet or particle in a moving continuous phase:

$$\overrightarrow{F_D} = \overrightarrow{F_G} - \overrightarrow{F_B} \quad (7)$$

(c) Microgravity

The third case represents a system in space. As it was not possible for us to conduct experiments in space, we can only consider this case with a theoretical approach. When travelling to space, the distance between a celestial body with

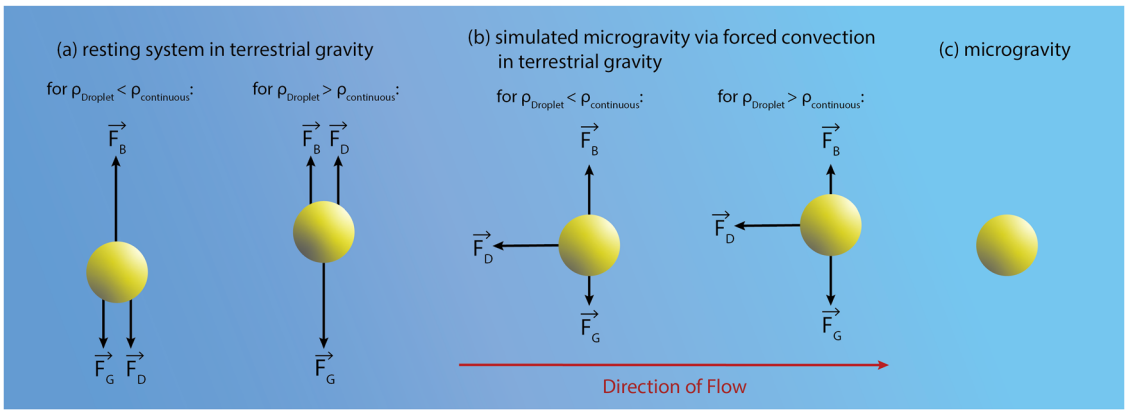

Fig. 4 Different forces ($\overrightarrow{F_B}$: buoyancy; $\overrightarrow{F_G}$: gravitational force; $\overrightarrow{F_D}$: drag force) acting on a droplet dispersed in a liquid for three different cases: (a) resting system with terrestrial gravity considering density differences between the two phases; (b) simulated microgravity in terrestrial gravity considering density differences between the two phases; (c) microgravity; $\rho_{droplet}$: density of the dispersed droplet; $\rho_{continuous}$: density of the continuous phase.

gravitational attraction and an object exposed to that attraction increases significantly, so that the resulting gravitational force according to Newton's law of universal gravitation decreases with distance. Eventually, the gravitational force becomes so small that it is negligible, *i.e.*, a state of weightlessness is reached. Therefore, gravity-induced emulsion instability mechanisms caused by density gradients, *i.e.*, creaming and sedimentation, are not a concern for emulsions in space. If temperature gradients are absent, droplet movement is determined by diffusion and Brownian motion and instability mechanisms are dominated by surface and viscous forces. Thus, any emulsion system on Earth in which surface and viscous forces dominate over gravitational forces can be comparable to a system in microgravity.

2.5. Characterisation of case (a): resting system in gravity

The movement of a droplet in an emulsion without forced convection, *i.e.*, a resting system, can be described *via* the stationary relative particle velocity $w_{d,rest}$ (relative to the velocity of the continuous phase), determined *via* the drag force in the balance of forces in eqn (6). As it is assumed that the droplets are of spherical shape, the gravitational force and the buoyancy can be defined according to eqn (8) and (9), respectively.

$$F_G = \rho_{droplet}\frac{4}{3}\pi {r_{droplet}}^3 g \quad (8)$$

$$F_B = \rho_{cont}\frac{4}{3}\pi {r_{droplet}}^3 g \quad (9)$$

The drag force acts in opposite direction of the movement of the droplet. If the spherical droplets move slowly and at constant speed through the continuous phase, the drag force can be obtained *via* Stokes' law (eqn (10)). In this case, the drag force is referred to as Stokes' drag F_d, which applies for spheres moving at stationary, terminal velocity, *i.e.*, $w_{d,rest}$, and very small Reynolds numbers through a viscous liquid.

$$F_d = 6\pi\mu_{cont} r_{droplet} w_{d,rest} \quad (10)$$

Inserting eqn (8)–(10) into eqn (6) and solving for $w_{d,rest}$ leads to eqn (11):

$$w_{d,rest} = \frac{\frac{2}{9}{r_{droplet}}^2 g\left(\rho_{cont} - \rho_{droplet}\right)}{\mu_{cont}} \quad (11)$$

Any directed droplet movement in gravity is therefore a result by density differences between the dispersed and the continuous phase. The droplet moves vertically downwards when the droplet's density is higher than the density of the continuous phase, and $w_{d,rest}$ is negative. In this case, $w_{d,rest}$ is the sedimentation velocity. The droplet moves vertically upwards when the droplet's density is lower than the density of the continuous phase, and $w_{d,rest}$ is positive. In this case, $w_{d,rest}$ is the creaming velocity.

The stationary relative particle velocity $w_{d,rest}$ has been calculated for terrestrial (g_{Earth} = 9.807 m s^{-2}), Martian (g_{Mars} = 3.71 m s^{-2}), and lunar gravity (g_{moon} = 1.62 m s^{-2}) using the data set from our previous study. Mars and the moon have been chosen due to their high interest in current and future space missions.[45]

2.6. Characterisation of case (b): simulated microgravity in terrestrial gravity

2.6.1. Characterising the flow in the continuous phase *via* the RPM platform velocity. The dimensionless location coordinates of the RPM movement recordings were multiplied by the radius of platform's rotation $r_{rotation}$ to obtain location coordinates in metre. The location coordinates allowed then to calculate the length of the connection vector, which describes the movement of the platform from point A to point B within Δt if it moved the direct way, see eqn (13).

$$A = \begin{pmatrix} a_{1,1} \\ a_{2,1} \\ a_{3,1} \end{pmatrix} = r_{rotation}\begin{pmatrix} x_1 \\ y_1 \\ z_1 \end{pmatrix}; B = \begin{pmatrix} b_{1,2} \\ b_{2,2} \\ b_{3,2} \end{pmatrix} = r_{rotation}\begin{pmatrix} x_2 \\ y_2 \\ z_2 \end{pmatrix} \quad (12)$$

$$\left|\overrightarrow{AB}\right| = \sqrt{(b_{1,2} - a_{1,1})^2 + (b_{2,2} - a_{2,1})^2 + (b_{3,2} - a_{3,1})^2} \quad (13)$$

The length of the connection vector allows to calculate the angle α between point A and point B to the centre of the inner frame using the law of cosines, see eqn (14).

$$\alpha = \cos^{-1}\left(\frac{\left|\overrightarrow{AB}\right|^2 - 2{r_{\text{rotation}}}^2}{-2{r_{\text{rotation}}}^2}\right) \quad (14)$$

The angle α allows to calculate the circular arc L *via* eqn (15), on which the platform moves from point A to point B.

$$L = \alpha \pi r_{\text{rotation}} \quad (15)$$

It is assumed that the velocity of the platform movement between point A to point B is constant, as the measurement time intervals are sufficiently small with 1.1 s. Therefore, the circular arc L was divided by Δt to obtain the velocity of the platform between point A and point B:

$$v_{A\to B} = \frac{L}{\Delta t} := w_{\text{cont}} \quad (16)$$

The emulsion sample vials (see Fig. 5(a)) on the RPM's experimental platform move with the same velocity as the platform. Due to the low viscosity of the aqueous phase, it is assumed that the velocity of the vial directly translates to the velocity of the aqueous phase, and any drag is negligible. At the same time, turbulences caused by back flow of the aqueous phase are neglected. Thus, the flow velocity of the aqueous (continuous) phase w_{cont} is dependent on the radius of platform movement (can be varied *via* the fixtures) and the distance, that the platform covers within Δt (can be varied *via* the motion modes). w_{cont} was determined for each time interval Δt of the 24 h run of the RPM. The average flow velocity of the aqueous phase $w_{\text{cont, average}}$ was then calculated excluding the RPM's ramp-up phase.

$$w_{\text{cont,average}} = \frac{1}{n_t^*}\sum_{i=1^*}^{n_t^*} w_{\text{cont}} \quad (17)$$

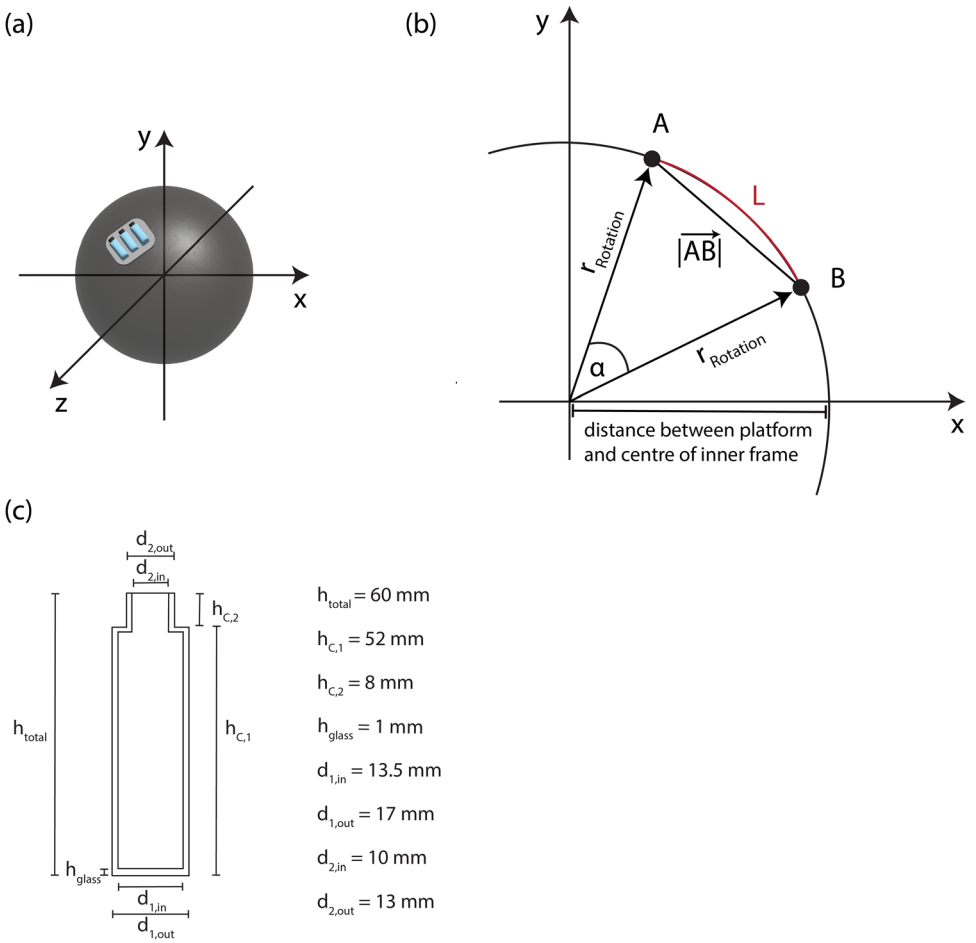

Fig. 5 Due to the 2-frame setup of the RPM, vials installed on the experimental platform move along a sphere around the centre of the inner RPM frame: (a) shows the sphere with the centre at (0|0|0); (b) shows how to calculate the circular arc L on which the RPM platform travels from A to point B within the time interval Δt (for simplicity in 2D), (c) shows the dimensions of the sample vial.

The flow regime in the continuous phase can be determined *via* the Reynolds number:

$$\mathrm{Re}_{\mathrm{cont}} = \frac{w_{\mathrm{cont,average}} h \rho_{\mathrm{cont}}}{\mu_{\mathrm{cont}}} \quad (18)$$

The characteristic length h needs to be defined for the different motion modes. In case of the 0 g and 0.4 g, the RPM moves constantly in different directions, changing the direction of fluid flow constantly, as well as the associated geometry. For simplicity, only the smallest and largest characteristic length are considered for calculating the Reynolds number, excluding the screw top of the vial. For the smallest characteristic length, the fluid flows parallel to the long side of the vial, resembling a circular pipe. Therefore, the characteristic length is the inner diameter of the vial ($d_{1,\mathrm{in}}$). For the largest characteristic length, the fluid flows parallel to the short side of the vial, resembling a rectangular duct at the cross-sectional area. Thus, the characteristic length is the hydraulic diameter d_{hyd} (eqn (19)).

$$d_{\mathrm{hyd}} = \frac{4A_{\mathrm{Duct}}}{U_{\mathrm{Duct}}} \quad (19)$$

In the case of the clinostat motion setting, the circular movement of the platform is carried out only around the z-axis. As the vials are lying on the platform, the fluid flow can only take place in parallel to the short side of the vial. Therefore, only the hydraulic diameter is used to calculate the Reynolds number for the clinostat motion setting.

2.6.2. Determining the impact of shear forces on the droplets. The forced movement of the aqueous phase, *i.e.*, the forced convection induced by the movement of the RPM, is acting in form of shear forces on the oil droplets. To determine the impact of shear forces on the droplets, the work $\Delta W_{\mathrm{shear}}$ induced by the shear forces on one dispersed droplet is compared to the free energy of emulsion formation ΔG_{Form}, that would be required to split the droplet into two droplets of the same size. If $\Delta W_{\mathrm{shear}}$ is larger than ΔG_{Form}, the droplet size decreases.

$$\Delta W_{\mathrm{shear}} > \Delta G_{\mathrm{Form}} \quad (20)$$

$\Delta W_{\mathrm{shear}}$ is a product of the shear force and the droplet diameter. Assuming that the oil phase of the droplets is a Newtonian liquid, $\Delta W_{\mathrm{shear}}$ can be determined *via* eqn (21).

$$\Delta W_{\mathrm{shear}} = F_{\mathrm{S}} d_{\mathrm{droplet}} = \mu_{\mathrm{droplet}} \dot{\gamma} A_{\mathrm{droplet}} d_{\mathrm{droplet}} \quad (21)$$

The shear rate $\dot{\gamma}$ can be obtained by dividing the flow velocity of the aqueous phase with the characteristic length, in this case the droplet diameter d_{droplet}.

$$\dot{\gamma} = \frac{w_{\mathrm{cont,average}}}{d_{\mathrm{droplet}}} \quad (22)$$

To obtain ΔG_{Form}, it is assumed that the process of the spontaneous emulsification is completed, *i.e.*, the diffusion of the surfactant from the bulk of the oil phase to the droplet interface is completed and there is no further decrease in particle size. ΔG_{Form} is defined according to eqn (23). Typically, the change of entropy in the system is considerably smaller than the change in free energy of the interface. Therefore, it is assumed that ΔS is negligible compared to ΔW. For $\Delta A_{\mathrm{surface}}$, it is assumed that the droplets split into two droplets of the same volume. Therefore, ΔG_{Form} is dependent to the surface tension σ and the increase of surface area $\Delta A_{\mathrm{surface}}$ of the newly formed droplets.

$$\Delta G_{\mathrm{Form}} = \Delta W - T\Delta S \approx \Delta W = \sigma \Delta A_{\mathrm{surface}} \quad (23)$$

J. Komaiko and D. J. McClements demonstrated that measuring the interfacial tension between the oil phase (medium chain triglycerides and Tween surfactant) and an aqueous phase (buffer solution) *via* a droplet shape analysis device is difficult, as even low polysorbate 80 concentrations lead to a loss of the pendant drop shape of the oil phase when immersed in the aqueous phase.[40] Therefore, for calculating the free energy of emulsion formation, the literature value of the interfacial tension between only medium chain triglycerides and a buffer solution (0.0282 N m^{-1})[40] is used for determining ΔG_{Form}.

2.6.3. Determining the stationary relative particle velocity *via* the drag force. It is assumed that within Δt the movement of the platform is stationary, *e.g.*, the platform moves at a constant velocity without accelerating or slowing down. Therefore, the droplet movement within Δt is stationary. In this case, the drag force F_{D} for a spherical droplet can be obtained *via* eqn (24):[46]

$$F_{\mathrm{D}} = \zeta \rho_{\mathrm{cont}} \frac{\pi}{4} {d_{\mathrm{droplet}}}^2 \frac{{w_{\mathrm{d,conv}}}^2}{2} \quad (24)$$

The stationary relative droplet velocity $w_{\mathrm{d,conv}}$ describes how fast the droplets move in relation to the velocity of the aqueous phase. Taking eqn (7) into account, $w_{\mathrm{d,conv}}$ can be calculated *via* the equation of droplet motion:[46]

$$w_{\mathrm{d,conv}} = \sqrt{\frac{4}{3} g_{\mathrm{Earth}} d_{\mathrm{droplet}} \frac{\left|\rho_{\mathrm{droplet}} - \rho_{\mathrm{cont}}\right|}{\zeta \rho_{\mathrm{cont}}}} \quad (25)$$

The absolute droplet velocity $w_{\mathrm{d,abs}}$ is obtained by adding the stationary relative droplet velocity to the velocity of the continuous phase.[46]

$$\vec{w}_{\mathrm{d,abs}} = \vec{w}_{\mathrm{d,conv}} + \vec{w}_{\mathrm{cont}} \quad (26)$$

The drag coefficient is essential in determining the stationary relative droplet velocity. For fluid particles, the drag coefficient is typically experimentally determined, as the movable phase boundary surface and the occurrence of internal fluid circulations makes it difficult to establish a valid correlation. However, as the drag coefficient is a function of the Reynolds number for particles Re_{p}, which describes the flow regime immediately surrounding dispersed particles, there are two approaches in determining the drag coefficient for our system:

(i) Drag coefficient for a quasi-solid droplets

Since the surfactant accumulates at and stabilises the water/oil interface in our emulsion system, it is assumed that the oil droplets are quasi-solid particles with a rigid surface and no internal fluid circulation. For spherical solid particles in a

flowing fluid, the Reynolds number can be obtained *via* eqn (27):[46]

$$\mathrm{Re}_{\mathrm{p,solid}} = 18\left(\sqrt{1+\frac{\sqrt{\mathrm{Ar}}}{9}}-1\right)^2 \tag{27}$$

The Archimedes number is defined as follows:

$$\mathrm{Ar} = \frac{\left|\rho_{\mathrm{droplet}}-\rho_{\mathrm{cont}}\right|}{\rho_{\mathrm{cont}}}\frac{g_{\mathrm{Earth}}{d_{\mathrm{droplet}}}^3}{{\nu_{\mathrm{cont}}}^2} \tag{28}$$

For $\mathrm{Re_p} \ll 1$, a creeping flow (= Stokes flow) prevails. At Stokes flow, the flow streamlines in front and behind the particle in flow direction are symmetrically identical, whereas above $\mathrm{Re_p} = 0.1$, the flow streamlines lose their symmetry, and at $\mathrm{Re_p} = 20$, the flow streamlines detach from the particle's downstream side to form stationary, laminar ring vortices. At Stokes flow, the drag coefficient for solid particles is reciprocally dependant on $\mathrm{Re_{p,solid}}$:[47]

$$\zeta_{\mathrm{solid}} = \frac{24}{\mathrm{Re}_{\mathrm{p,solid}}} \tag{29}$$

(ii) Drag coefficient for liquid droplets

As approach (i) determined a Stokes flow in the liquid surrounding the dispersed quasi-solid particles, it is assumed that the same flow regime prevails for fluid particles, too. For a Stokes flow, the Navier–Stokes-equation can be solved using a theoretical approach, leading to eqn (30) for the drag coefficient for liquid droplets.[48,49]

$$\zeta_{\mathrm{liquid}} = \frac{24}{\mathrm{Re}_{\mathrm{p,liquid}}}\frac{\frac{2}{3}+\frac{\mu_{\mathrm{droplet}}}{\mu_{\mathrm{cont}}}}{1+\frac{\mu_{\mathrm{droplet}}}{\mu_{\mathrm{cont}}}} \tag{30}$$

Solving the equation of droplet motion (eqn (25)) for the Archimedes number (as described in eqn (28)) leads to an alternative definition of the Archimedes number:

$$\mathrm{Ar} = \frac{3}{4}{\mathrm{Re}_{\mathrm{p,liquid}}}^2\zeta_{\mathrm{liquid}} \tag{31}$$

Inserting eqn (30) into eqn (31) allows to determine the Reynolds number for liquid particles, and subsequently the drag coefficient.

2.6.4. Scaling law analysis. Scaling law analysis allows to evaluate the impact of the different forces (gravitational force, surface tension forces, natural convection, forced convection, viscous forces) on the dispersed droplets. In this case, the Bond number, the Richardson number, and the Grashof number are considered.

The Bond number (sometimes referred to as Eötvös number) describes the ratio of gravitational forces to surface tension forces.

$$\mathrm{Bo} = \frac{g_{\mathrm{Earth}}\Delta\rho{d_{\mathrm{droplet}}}^2}{\sigma} \tag{32}$$

The Richardson number describes the ratio of natural convection to forced convection. Both approach (i) and (ii) are considered for $\mathrm{Re_p}$.

$$\mathrm{Ri} = \frac{\mathrm{Gr}}{{\mathrm{Re_p}}^2} \tag{33}$$

The Grashof number Gr is defined *via* eqn (34).

$$\mathrm{Gr} = \frac{g_{\mathrm{Earth}}\beta\left(T_{\mathrm{droplet}}-T_{\mathrm{cont}}\right){d_{\mathrm{droplet}}}^3}{{\nu_{\mathrm{cont}}}^2} \tag{34}$$

The linear expansion coefficient β is defined as:

$$\beta = -\frac{1}{\rho_{\mathrm{cont}}}\left(\frac{\delta\rho}{\delta T}\right)_{\mathrm{p}} \cong -\frac{1}{\rho_{\mathrm{cont}}}\left(\frac{\rho_{\mathrm{cont}}-\rho_{\mathrm{droplet}}}{T_{\mathrm{cont}}-T_{\mathrm{droplet}}}\right) \tag{35}$$

Solving eqn (35) for the term $\beta\left(T_{\mathrm{droplet}}-T_{\mathrm{cont}}\right)$ and inserting it in eqn (34) leads to an expression of the Grashof number, which is adjusted for mass transfer, *i.e.*, describes natural convection caused by concentration gradients instead of temperature gradients.

$$\mathrm{Gr} = \frac{\Delta\rho g_{\mathrm{Earth}}{d_{\mathrm{droplet}}}^3}{\rho_{\mathrm{cont}}{\nu_{\mathrm{cont}}}^2} \tag{36}$$

2.7. Workflow

As summary, Fig. 6 visualises the different steps undertaken to evaluate the presented system. Arrows indicate the input of data required for each step.

3. Results and discussion

3.1. Assessment of the simulated microgravity of a random positioning machine

The simulated gravity decreased quickest using any of the clinostat motion modes than the 0 g or 0.4 g motion mode (approx. 6 min compared to approx. 25 min, see Fig. 7(a)). This shows that simulating microgravity *via* movement is only suited for slow processes, where the initial start-up phase is negligible. At the centre of rotation, the 0 g motion mode simulated microgravity at a magnitude of 10^{-3} g, while the clinostat motion modes reached lower simulated microgravity at a magnitude of 10^{-4}–10^{-5} (see Fig. 7(b)). Both the faster decrease in simulated gravity and the lower values for microgravity are caused by the clinostat motion mode's significantly higher frame speed of 80–120 deg s^{-1}, as set by the operator prior to experimentation. In comparison, the 0 g and 0.4 g motion modes were pre-set at maximum frame speeds of 15 deg s^{-1} (random speed) according to their motion path files. For the clinostat motion mode, a frame speed of 80 deg s^{-1} reached overall the lowest average simulated microgravity of 5.1×10^{-5} g, however, with a standard deviation of 6.4×10^{-5} g, it showed the widest spread in simulated microgravity (see Fig. 7(a)). Standard deviation was considerably lower at clinostat motion modes at 100–120 deg s^{-1}, and values for average simulated microgravity indicate a slight decrease with increased frame speeds.

Considering the influence of an off set of an experimental vessel to the centre of rotation, the simulated microgravity

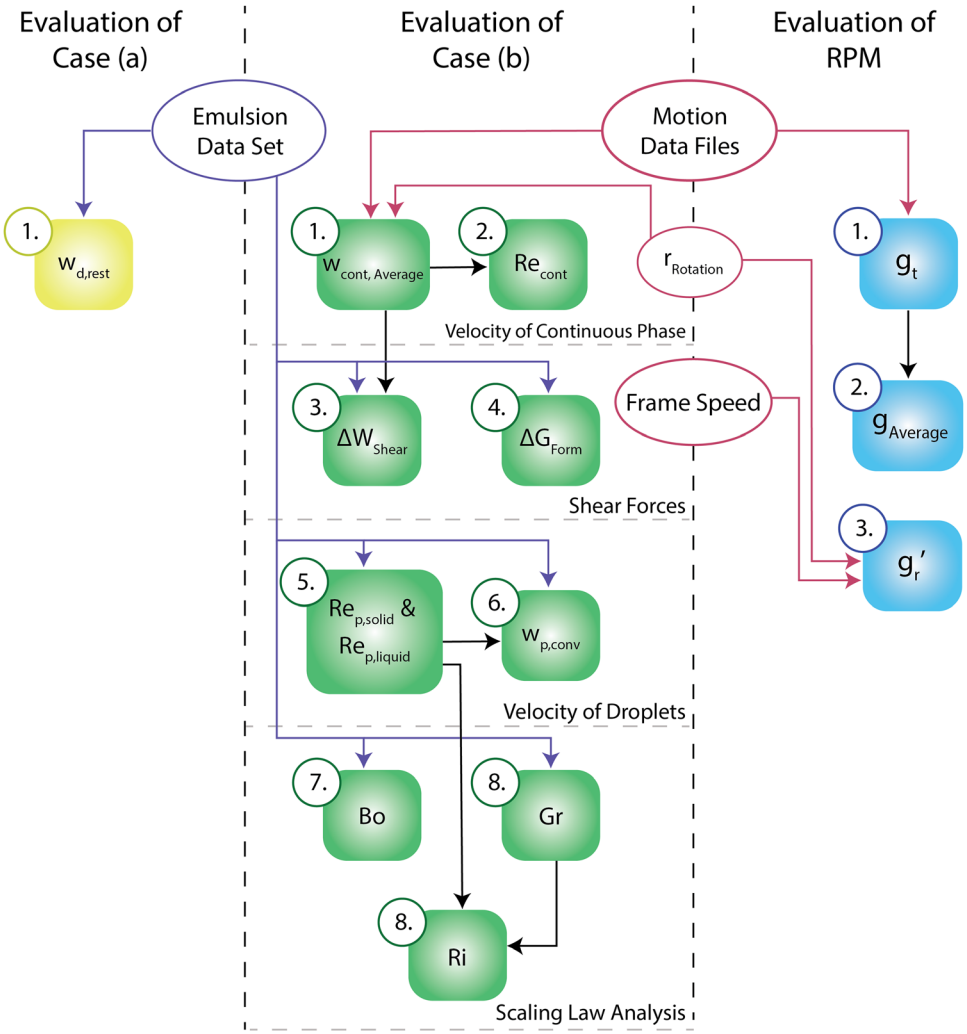

Fig. 6 Visualisation of the workflow of the steps undertaken to evaluate the droplet movement in a system at rest (case a) and in a system with forced convection caused by the random positioning machine (case b) as well as the microgravity simulated by the random positioning machine; arrows indicate the input of data for each step.

generally increased with increasing distance (see Fig. 7(c) and (d)). However, at a frame speed of 15 deg s^{-1}, g'_r was overall predicted to be considerably lower than the average simulated microgravity of the 0 g motion mode (see Fig. 7(c)). Yet, the function to determine g'_r only considers uniform movement at constant frame speeds, while both the 0 g and 0.4 g motion modes change their direction of movement and frame speed randomly to simulate anticipated gravity values. Thus, the g'_r function cannot distinguish between the 0 g and the 0.4 g motion mode and offers only limited informative value in these cases. For the clinostat motion mode, g'_r was overall predicted higher than at the centre of the rotation and g'_r increased with increasing frame speed at a given $r_{rotation}$ (see Fig. 7(d)). Even though there is a considerate increase in simulated microgravity in the form of several magnitudes with increasing distance to the centre of rotation and increasing frame speed, even in a worst-case scenario at a radius of 7.5 cm (fixture (e), see Fig. 1(c)), the simulated microgravity is with approx. 0.03 g still considerably below 0.1 g. Still, due the significant changes in simulated microgravity with $r_{rotation}$, the findings indicate that size and placement of the sample vessel are important factors for microgravity studies, aligning with previous research.[15]

3.2. Characterisation of case (a): resting system in gravity

The relative stationary droplet velocity $w_{d,rest}$ decreases with decreasing droplet diameter (see Fig. 8(a)). As the droplet diameter decreases, the droplet density increases due to a higher surfactant concentration which drives self-assembly of the smaller droplets. At very small droplet diameters, the droplet velocity is negative, leading to sedimentation. With increasing droplet size, the droplet velocity increases and has positive values as soon as the droplet density is smaller than the density of the aqueous phase, leading to creaming (d_{32} approx. 200 nm). Above droplet diameters of 10 μm, the droplet velocity increases rapidly. For a given droplet diameter, the droplet velocity decreases with decreasing gravity, as the buoyancy and the gravitational force decrease with decreasing gravity (see Fig. 8(a) and (b)).

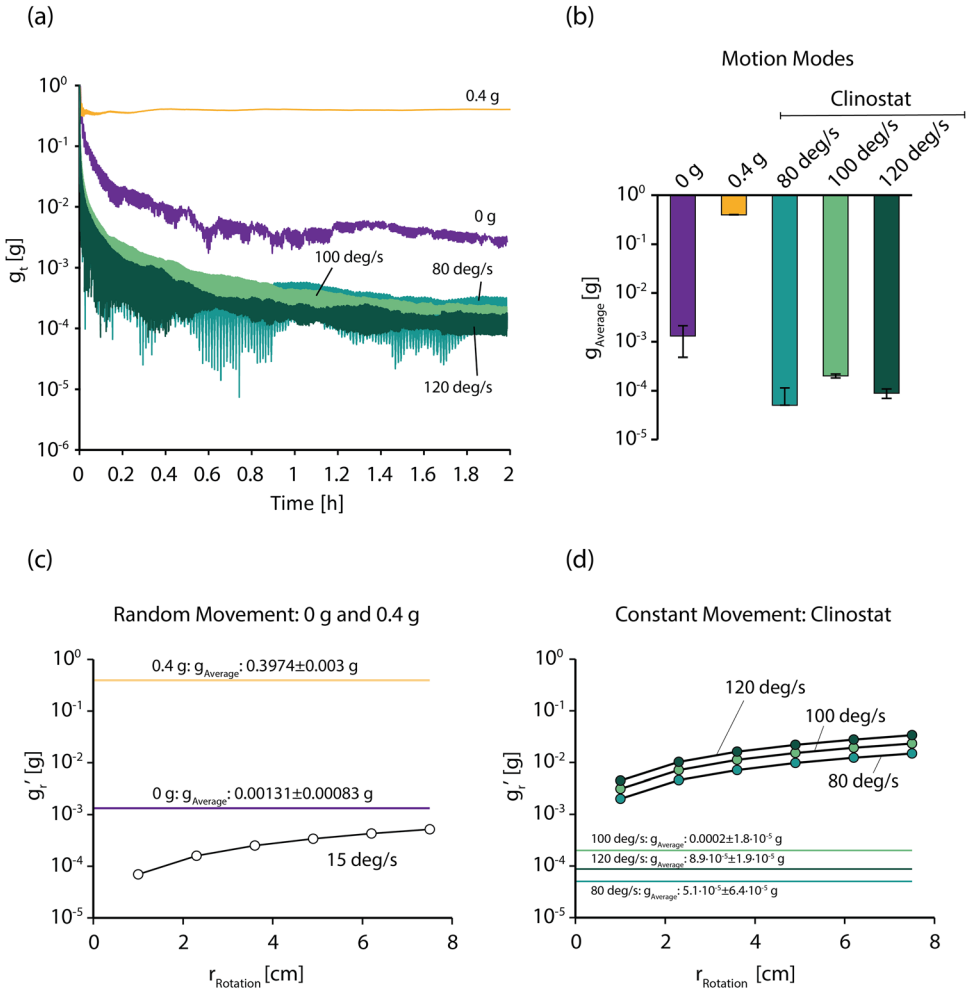

Fig. 7 (a) Simulated gravity g_t of 5 RPM motion modes (0.4 g, 0 g, clinostat at 80 deg s^{-1}, 100 deg s^{-1}, and 120 deg s^{-1}) over the first two hours after starting the RPM; (b) simulated gravity $g_{average}$ averaged over the RPM run (24 h) excluding the ramp-up phase (1st hour) for the different RPM motion modes; (c) simulated microgravity g'_r in relation to radius r to the centre of rotation for a frame rate of 15 deg s^{-1}; (d) simulated microgravity g'_r in relation to radius r to the centre of rotation for a frame rate of 80–120 deg s^{-1}.

In theory, the most stable emulsion can therefore be achieved when the dispersed phase has the same density as the continuous phase, as the droplet would not be affected by gravitational forces. In practicality, the impact of gravitational forces on the droplet can be disregarded at creaming/sedimentation velocities of 1 mm day^{-1} or 0.0116 µm s^{-1},[50] depicted as the critical droplet velocity $w_{d,critical}$ in Fig. 8(b). For our system in terrestrial gravity, droplets with droplet diameters below approx. 1.3 µm (= critical droplet diameter, *i.e.*, droplet diameter at $w_{d,critical}$) reach droplet velocities below the critical droplet velocity, and can therefore be considered unaffected by gravitational forces, *i.e.*, the instability mechanisms sedimentation and creaming. Droplet movement occurs undirected *via* Brownian motion, which can cause coalescence of colliding droplets, *i.e.*, Brownian flocculation.[50]

Thus, our findings demonstrate that for our emulsion system, a critical droplet diameter of 1.3 µm and below in a system at rest would be suitable to simulate microgravity, avoiding the use of specific equipment. In general, the critical droplet diameter is dependent on the viscosity of the continuous phase and the differences in density between the continuous and dispersed phase (see eqn (11)). For our model system at droplet diameters of 1.3 µm and below, the differences in density are comparatively low. For dispersed systems with greater density differences, the critical droplet diameter decreases, requiring overall smaller particles for a microgravity analogous and making the use of specific equipment for microgravity simulation more likely.

3.3. Characterisation of case (b): simulated gravity in terrestrial gravity

3.3.1. Characterising the flow in the continuous phase. All determined velocities of the continuous phase w_{cont} showed a considerate variability over time (see Fig. 9(a) and (b)). This is expected for 0 g and 0.4 g motion modes due to their mode of operation of changing frame speed between time intervals (random movement), however unexpected for the clinostat modes, indicating that the RPM might not be able to hold a

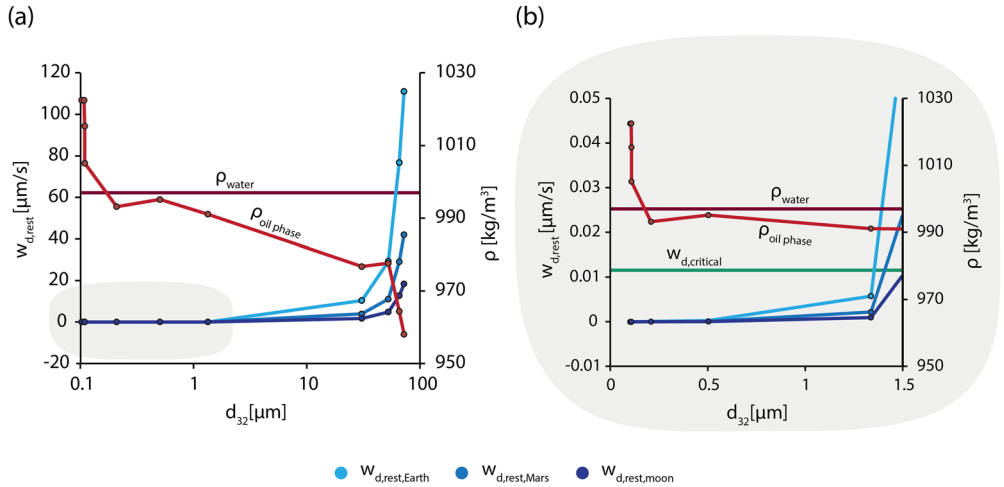

Fig. 8 Relative stationary droplet velocity $w_{d,rest}$ in a resting system (primary y-axis) for terrestrial gravity (9.807 kg m^{-3}), Martian gravity (3.71 kg m^{-3}), and lunar gravity (1.62 kg m^{-3}) and the density (secondary y-axis) of both phases (density of oil phase = $\rho_{droplet}$; density of aqueous phase = $\rho_{cont.}$) in relation to the particle diameter d_{32} with (a) showing the whole range and (b) focusing on the area of very small $w_{d,rest}$ for comparison with $w_{d,critical}$.

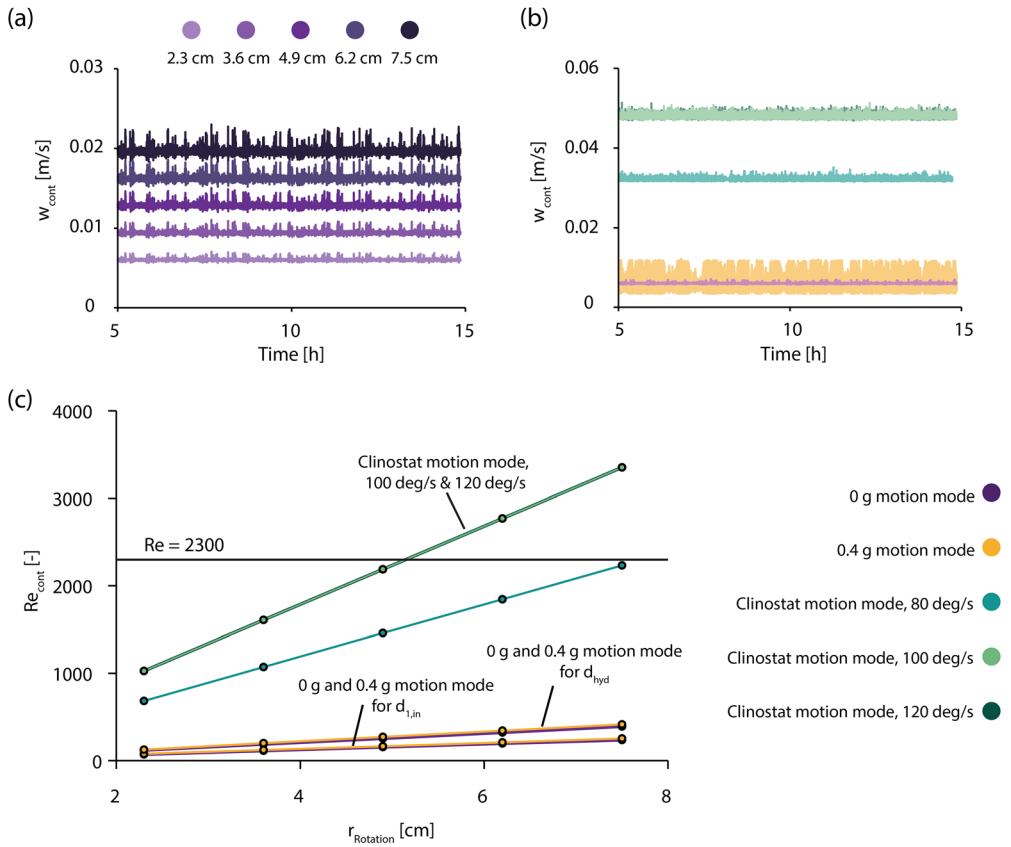

Fig. 9 Platform velocity in relation to time for (a) increasing radius of platform movement at a RPM motion mode for 0 g and (b) at a radius of platform movement of 2.3 cm with different RPM motion modes (0 g, 0.4 g, clinostat 80 deg s^{-1}, clinostat 100 deg s^{-1}, clinostat 120 deg s^{-1}); (c) Reynolds numbers of the continuous phase Re_{cont} in relation to the radius of platform movement for 5 different RPM movement motion modes (0 g; 0.4 g; clinostat 80 deg s^{-1}; clinostat 100 deg s^{-1}; clinostat 120 deg s^{-1}). For 0 g and 0.4 g motion mode: lower and upper Reynolds numbers of the continuous phase have been calculated based on the lower and upper characteristic lengths of the experimental vials resulting from the constant change in direction of the fluid flow. The vial's lower and upper characteristic lengths have been determined by simplifying the vial's geometry to a pipe (flow parallel to the vial's long side) and duct geometry (flow parallel to the vial's short side), respectively. The area between the upper and lower Reynolds numbers represents Reynolds numbers that occur when the direction of flow is at an angle, as the RPM platform can move in any direction during its run. For clinostat motion mode: circular motion around the z-axis, the Reynolds number has been calculated for the hydraulic diameter, as the fluid flow can only occur in parallel to the short side of the vial.

constant frame speed, and might be the reason for the observed variance in simulated microgravity in Section 3.1.

In general, w_{cont} increased with increasing radius of rotation, as it increases the distance the platform moves within a time interval (see Fig. 9(a)). The motion modes for 0 g and 0.4 g led to similar w_{cont}. In comparison, values for w_{cont} were at a significantly higher level using the clinostat motion modes. w_{cont} is expected to increase with increasing frame speed of the clinostat motion mode, yet frame speeds of 100 deg s^{-1} and 120 deg s^{-1} led to same values considering experimental error (4.82 cm s^{-1}). This indicates that the frame speed of 120 deg s^{-1} was not met, *i.e.*, the RPM is not able to reach frame speeds above 100 deg s^{-1} although giving the option in the software.

The Reynolds number of the continuous phase Re_{cont} in relation to the radius of circular movement was determined *via* the velocity of the continuous phase averaged over time $w_{cont,average}$. Both the 0 g and 0.4 g motion mode led to very similar Re_{cont} in the range of 70–420, increasing with the radius of platform movement. Therefore, Re_{cont} are well below the critical Reynolds number of 2300 (pipe geometry) and laminar flow is present under all circumstances in both the 0 g and 0.4 g motion mode.

In case of the clinostat motion mode, the Re_{cont} increased significantly with both circular motion radius and set frame speed, although Re_{cont} for frame speeds of 100 and 120 deg s^{-1} were almost identical (see Fig. 9(c)), implying again that the RPM cannot reach frame speeds above 100 deg s^{-1}. In most circumstances, laminar flow is present in the vials. However, the combination of high circular motion radii with frame speeds of 100–120 deg s^{-1} led to flow regimes in the transition region between laminar and turbulent flow ($Re > 2300$). In this region, the flow streamlines of the continuous phase lose their symmetry, with the flow fluctuating in velocity and pressure while small addies can form. Dispersed particles might be exposed to more movement compared to the laminar flow regime, causing the effect of forced convection from the RPM's movement to multiply (*e.g.*, forces acting on the droplets), even without considering the effect of any turbulences caused by drag or back flow. It is therefore advisable to avoid a transitional flow in liquid samples for simulated microgravity studies, *i.e.*, avoid high fame speeds in microgravity simulations.

3.3.2. Determining the impact of shear forces on the droplets. The work ΔW_{shear} induced by shear forces on one dispersed droplet is dependent on both RPM experiment parameters (motion mode and radius of platform movement influence platform velocity leading to higher shear forces, see eqn (16) and (21)) and droplet characteristics (cross-sectional area of the droplet and viscosity of the oil phase, see eqn (21)).

Within an RPM motion mode, ΔW_{shear} increases continuously with increasing radius of platform movement (see Fig. 10(a)). Yet, in general, the motion mode as a greater influence on ΔW_{shear} than the radius of platform movement: while ΔW_{shear} is in the same range for both 0 g and 0.4 g motion mode, it increases significantly with the clinostat setting. Within the clinostat setting, ΔW_{shear} increases with increasing frame speeds due to the significantly higher platform velocities. However, based on their similar platform velocity, clinostat settings with 100 deg s^{-1} and 120 deg s^{-1} show no change in ΔW_{shear}.

In the SOR range of 0.75–1.5, the surfactant content is independent on the droplet size (approx. 100 nm) as the viscosity of the oil phase decreases, leading to a decrease in ΔW_{shear} (see Fig. 10(c)). Between droplet diameters of 108 nm (SOR = 0.75) to droplet diameters of 53 μm (SOR = 0.25) ΔW_{shear} increases logarithmically with a logarithmic increase in droplet diameter. In this area, there is a direct correlation between viscosity decrease and droplet size increase due to the decreasing surfactant content. At surfactant content below an SOR of 0.25 (= droplet diameters of 50–70 μm), ΔW_{shear} is approximately constant, as the decrease in surfactant content is approximately linear to the increase in droplet diameter in this area.

Comparing ΔW_{shear} to the resulting free energy of emulsion formation ΔG_{Form}, ΔW_{shear} is lower than ΔG_{Form} in most cases (see Fig. 10(c)). Therefore, the average droplet size would mostly not be influenced by the shear forces present. Only at small droplet diameters of approx. 100 nm in combination with clinostat settings of 100–120 deg s^{-1} and radii of platform movement of 4.9–7.2 cm or a clinostat setting of 80 deg s^{-1} and 7.5 cm radius of platform movement, is ΔG_{Form} equal or smaller than ΔW_{shear} (see Fig. 10(b)). In this case, the shear forces acting on the droplet would potentially be sufficient to split an oil droplet into two droplets, representing a serious corruption of experiments conducted in simulated microgravity. However, in this case the surface tension was only estimated with the value of the pure oil without surfactant present. Considering that the addition of surfactant in general lowers the surface tension at the oil–water interface, the true free energy of emulsion formation might be below the determined values and therefore also larger droplets could be affected by the shear forces present. Even prior to any change in average droplet size, shear forces might be large enough to change the shape of the droplets, which would also represent a serious corruption in study design. Experimental studies are required to confirm the influence of shear forces caused by forced convection on the droplet characteristics.

Thus, even though the clinostat motion modes can simulate lower microgravities while reaching anticipated values considerably quicker, they come with a trade-off of a transitional flow regime and higher shear forces acting on dispersed particles. Excessive shear forces, potentially present at high frame speeds in combination with large radii of circular movement, might be able to affect the average particle size or particle shape. These conditions should be avoided when planning studies in simulated microgravity to avoid a corruption of study findings.

3.3.3. Stationary relative particle velocity. The stationary relative particle velocity $w_{d,conv}$ results from the interaction of the gravitational force, buoyancy, and drag force (as reaction to forced convection) on the dispersed droplet. Determination of $w_{d,conv}$ is, in case of Stokes flow, possible *via* the Reynolds number for particles Re_p which describes the flow pattern immediately surrounding the dispersed droplet (see Fig. 11(a)). In both approaches (i) and (ii) for quasi-solid particles and liquid

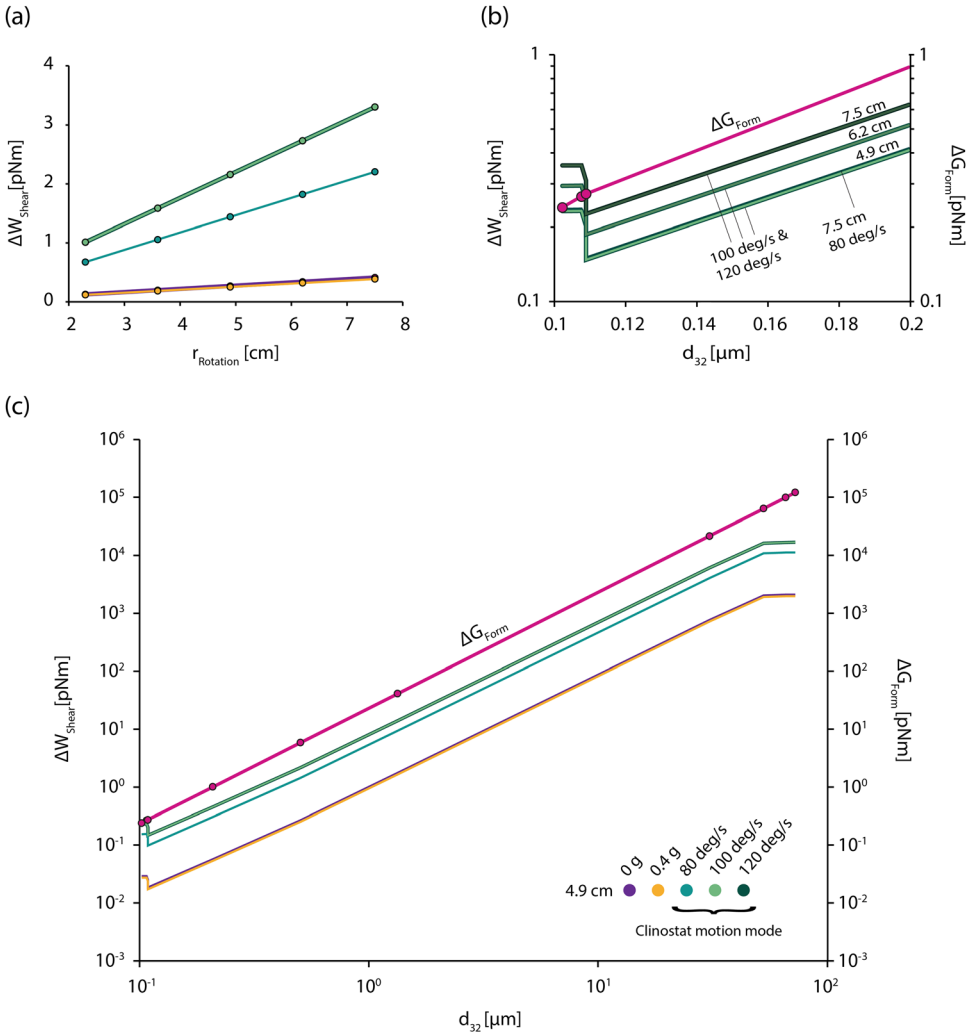

Fig. 10 (a) Work ΔW_{shear} induced by shear forces in relation to radius of platform movement r for an average droplet diameter of approx. 500 nm at a surfactant-to-oil ratio of 0.45 for 0 g motion mode, 0.4 g motion mode and clinostat motion mode (80 deg s^{-1}, 100 deg s^{-1}, 120 deg s^{-1}); (b) work ΔW_{shear} induced by shear forces (primary y-axis) and free energy of emulsion formation ΔG_{Form} (secondary y-axis) in relation to average droplet diameter d_{32} for 0 g motion mode, 0.4 g motion mode and clinostat motion mode (80 deg s^{-1}, 100 deg s^{-1}, 120 deg s^{-1}); (c) work ΔW_{shear} induced by shear forces (primary y-axis) and free energy of emulsion formation ΔG_{Form} (secondary y-axis) in relation to average droplet diameter d_{32} for 0 g motion mode, 0.4 g motion mode and clinostat motion mode (80 deg s^{-1}, 100 deg s^{-1}, 120 deg s^{-1}).

droplets, respectively, Re_p is a function of the Archimedes number, as the motion of dispersed particles is influenced by density differences of the dispersed and the continuous phase. For approach (i), $Re_{p,solid}$ ranges between approx. 5.7×10^{-12}–0.008 and increases with increasing droplet diameter. Thus, $Re_{p,solid}$ is below the critical Reynolds number of 0.1, below which a Stokes flow is prevalent around the particle. For approach (ii), $Re_{p,liquid}$ ranges between approx. 6.8×10^{-12}–0.01, confirming the assumption of Stokes flow. For liquid droplets in particular, the symmetrical flow streamlines of the continuous phase within a Stokes flow imply that droplets are likely to keep their spherical shape. Both approaches (i) and (ii) lead to values of $w_{d,conv}$ in the same order of magnitude in relation to the respective droplet diameter, and the trend of their resulting curves is identical due to their strong dependence on the droplet diameter (see Fig. 11(b)). However for all droplet sizes, the values of $w_{d,conv,liquid}$ based on approach (i) are approx. 20 ± 1.5% above $w_{d,conv,solid}$, based on approach (ii) with the difference slightly increasing with increasing droplet diameter. As it was not possible for us to confirm relative droplet velocities experimentally, it is concluded that both approaches seem to be valid to approximate the relative droplet velocity instead of giving exact values.

In general, $w_{d,conv}$ is considerably small for both approaches: the distance the droplets move within Δt relative to the movement of the continuous phase is below the droplets' diameter in most cases ($d_{32} < 60$ µm) (see Fig. 11(c)). Above a diameter of approx. 60 µm the movement of the droplets becomes more pronounced, as the distance droplets move within Δt is greater than the droplets' diameter, however, is still below twice the droplet diameter (108–134 µm at the largest droplet size, depending on the approach). Thus, in all cases is the droplet movement relative to the continuous phase very small.

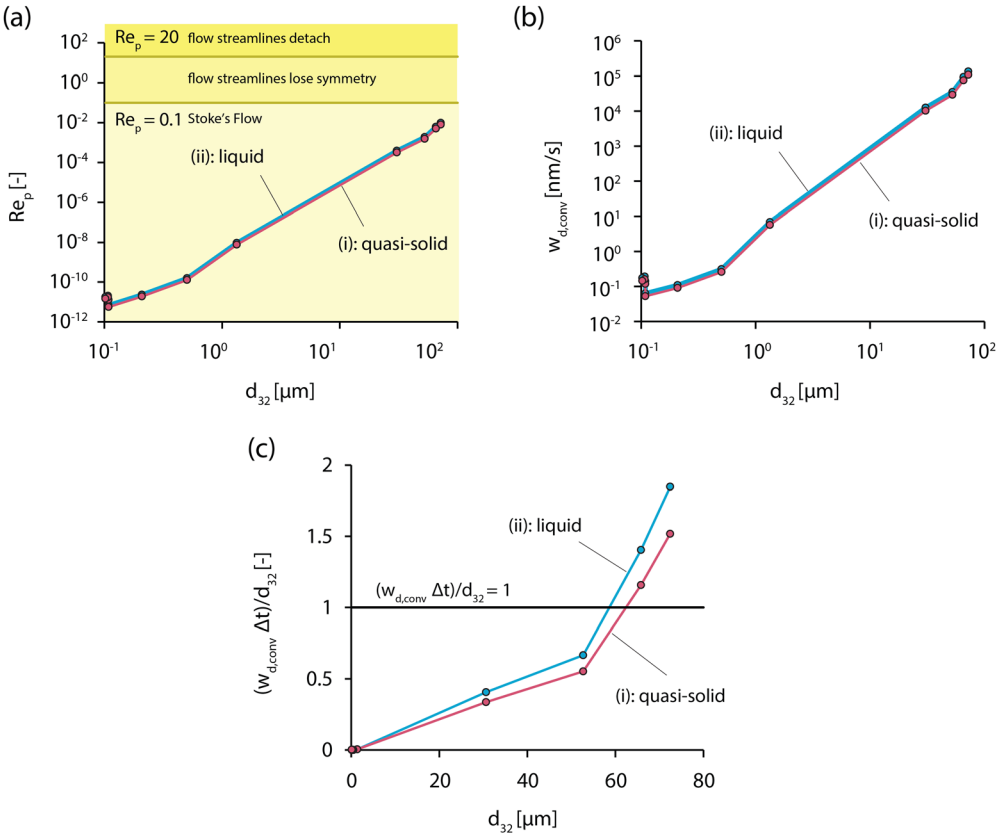

Fig. 11 (a) Reynolds number of the particle Re_p in relation to average droplet diameter d_{32}; (b) relative droplet velocity $w_{d,conv}$ in relation to average droplet diameter d_{32}; (c) ratio of relative droplet velocity $w_{d,conv}$ to average droplet diameter d_{32} in time interval Δt in relation to average droplet diameter d_{32}.

Droplets' movement might express itself as a trembling relative to the movement of the continuous phase. This would suggest that while the droplets get carried with the movement of the continuous phase, their movement relative to the continuous phase is negligible, similar to *e.g.*, a person sitting in a train.

The determination of $w_{d,conv}$ presented here is only applicable when a Stokes flow is present around the dispersed droplet, while it does not consider the flow regime in the continuous phase (see eqn (25)). However, since previous sections indicated a transitional flow regime and elevated shear forces in the clinostat mode at high frame rates, it is considered unlikely that a Stokes flow is present around the dispersed droplets under these conditions. Therefore, the findings on $w_{d,conv}$ are only considered likely for the 0 g and 0.4 g motion mode, where a laminar flow prevailed in the continuous phase. Still, the results need to be verified experimentally, as under all motion modes, the flow in the continuous phase has shown a strong variability, which might impact the stationary relative particle velocity. Additionally, since the direction of flow changes constantly for the 0 g and 0.4 g motion modes, the droplets might be more affected by drag and back-flow.

3.3.4. Scaling law analysis. The Bond number describes the ratio of the gravitational forces to the surface forces acting on the droplet for a static system, *i.e.*, assuming that flow-induced effects such as inertia are neglectable. In this case, the Bond number is ranging between 9.3×10^{-11} (SOR = 1.5) and 7.1×10^{-5} (SOR = 0.05). This is well below the critical Bond number of 1 (see Fig. 12(a)), which separates systems that are dominated by gravitational forces ($Bo \gg 1$) from systems that are dominated by surface forces ($Bo \ll 1$). Therefore, our model system, when simplified to an emulsion made of medium-chain triglycerides and a buffer solution (surface tension: 0.0282 N m^{-1}), is dominated by surface forces for all droplet diameters considered, and gravitational forces can be neglected. Adding surfactant to the system leads to a decrease in surface tension, and subsequently to an increase of the Bond number. To reach the critical Bond number, the surface tension would need to decrease to 1.64×10^{-12} N m^{-1} (SOR = 1.5) to 1.26×10^{-6} N m^{-1} (SOR = 0.05). It is considered unlikely that the amount of surfactant added to the oil phase could decrease the surface tension in such an extent that the critical Bond number is reached.

The Grashof number describes the ratio of natural convection in form of buoyancy in relation to viscous forces. Due to the assumption of constant temperature throughout the sample vial, the buoyancy is in this case driven by gravity-interactions with concentration gradients instead of temperature gradients (see eqn (35)). As the Grashof number is below the critical value of 1 for all droplet diameters (see Fig. 12(b)), viscous forces dominate over the buoyancy, and therefore gravitational forces.

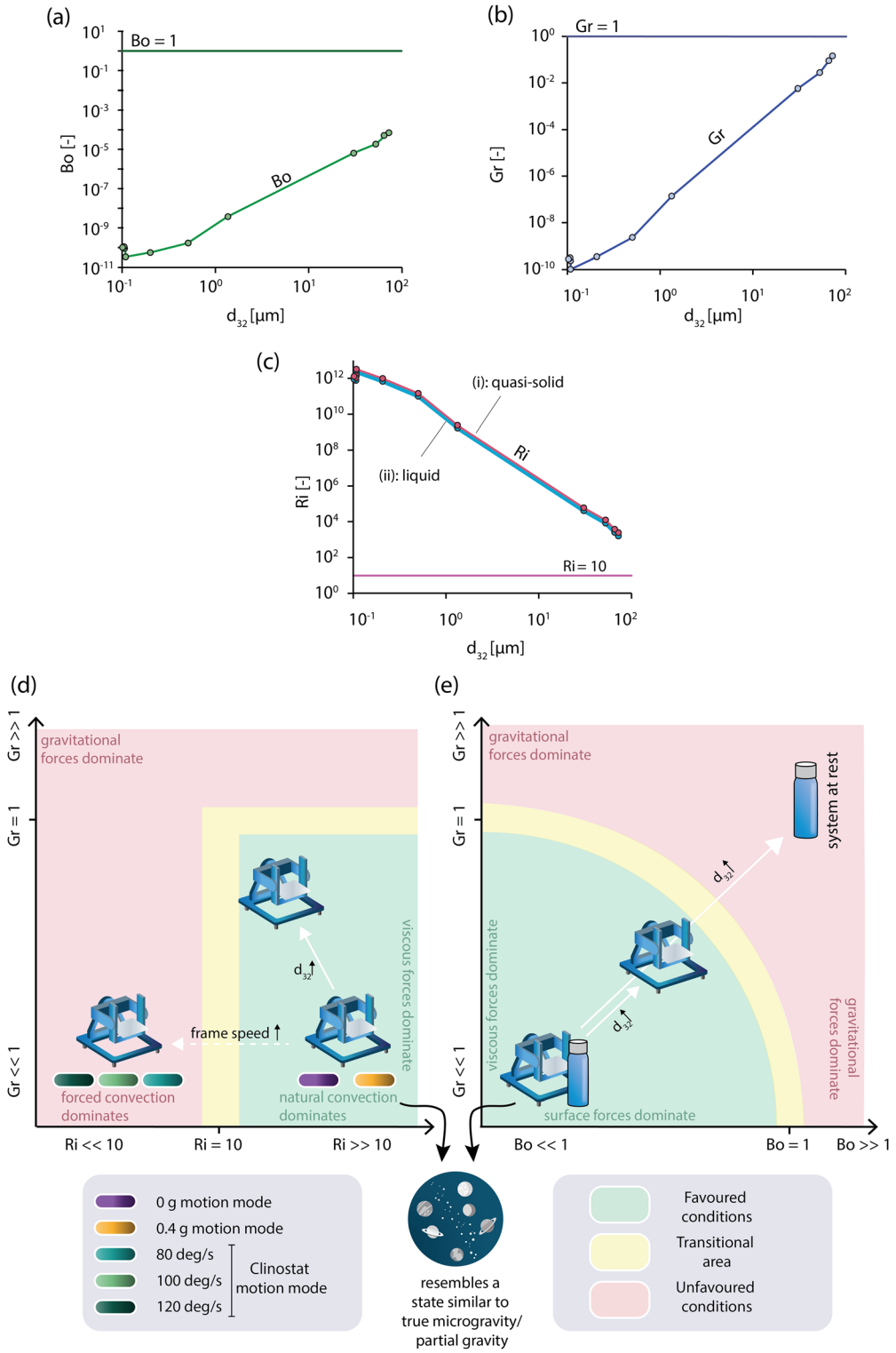

Fig. 12 (a) Bond number Bo in relation to average droplet diameter d_{32}; (b) Grashof number in relation to average droplet diameter d_{32}; (c) Richardson number Ri in relation to average droplet diameter d_{32}; (d) Grashof number Gr in relation to Richardson number Ri; (e) Grashof number Gr in relation to Bond number Bo.

The Richardson number is a ratio of Grashof number to the squared Reynolds number for particles, *i.e.*, a ratio of natural convection to forced convection. For both approach (i) and (ii), the Richardson number is well above the critical value of 10 (see Fig. 12(c)), at which natural convection dominates, and forced convection is negligible.

Setting all three dimensionless numbers in relation to each other (see Fig. 12(d) and (e)), the system can now be compared

to true microgravity in space. In space, liquid systems not exposed to forced convection would be dominated by viscous forces and surface forces, while natural convection, driven by gravity–density-interaction caused by temperature or concentration gradients, does not exist. For a microgravity simulation under gravity, natural convection must dominate over forced convection to avoid study corruption. To then minimize the effect of natural convection, viscous forces and surface forces must dominate over natural convection.

While viscous and surface forces dominate over gravitational forces for all droplet sizes on the RPM (depicted as RPM icon in Fig. 12(e)), for a liquid system at rest (depicted as vial icon in Fig. 12(e)), gravitational forces dominate over viscous and surface forces once the droplets exceed a certain size ($d_{32} >$ 1.3 μm). While a liquid system at rest might be a suitable analogue for some dispersed systems, an RPM is able to simulate microgravity for a larger range of systems. In this study, droplets of a size of up to 70 μm in diameter were suitable for the RPM and based on the trend of the Grashof and Bond number, even larger particles might be suitable. However, since emulsions of larger droplet sizes are more prone to instability mechanisms, there might be limitations stemming from the time scale of their instability mechanism. The time scale of emulsion instability mechanisms can be shorter than the time required by the RPM to simulate a microgravity-like effect on the dispersed droplets, rendering emulsions unsuitable for this type of microgravity simulation. To identify emulsions with droplet sizes suitable for the RPM, experimental studies are required.

Still, microgravity can only be sufficiently simulated if forced convection is negligible. While under laminar flow (continuous phase) in combination with Stokes flow (dispersed particles), this condition is met for all particle sizes (depicted as RPM icon in Fig. 12(d)), findings of the previous sections suggested that an increase in frame rates increases the Reynolds-number in the continuous phase which was associated with increased shear forces on the dispersed droplets (*i.e.*, loss of the droplet's spherical shape and/or influence on average droplet size) and potentially a lack of Stokes flow around the droplets. The authors therefore conclude that the clinostat motion mode under frame rates of 80–120 deg s^{-1} is at risk to be dominated by forced convection, thus not be able to simulate microgravity for dispersed systems with characteristics as considered here.

In conclusion, only the 0 g and 0.4 g motion mode can provide a suitable simulation of microgravity and partial gravity for experimental studies of dispersed systems on Earth. For future investigations, it is advisable to investigate the clinostat mode at low frame rates as well as other RPM motion modes (*e.g.*, random movement) at low frame rates. At the same time, experimental studies are required to confirm these findings.

4. Conclusions

Experimental parameters need to be chosen carefully to avoid corruption of findings of simulated microgravity studies. For emulsion studies using a random positioning machine (RPM 2.0 by Airbus/Yuri), we proposed a computational method to evaluate the quality of the simulated microgravity under different motion modes and identify potential shortcomings in study design. While we focus on an emulsion model system, our methods can also be applied to solid particles and cells, if certain characteristics (*e.g.*, density, particle size, *etc.*) of the dispersed phase are known. Similarly, our methods can be applied to other microgravity simulation devices of different dimensions and movement patterns, as long as they provide a logging option of their location coordinates.

While the clinostat motion mode at frame speeds of 80–120 deg s^{-1} reached stable microgravity values considerably quick (approx. 6 min), it came with a trade-off: the continuous phase is close to or in a transitional flow regime, generating potentially high shear forces on the dispersed droplet. These shear forces might change the shape of the droplets or even the average droplet size, which must not be mistaken for effects of simulated microgravity. The forced convection is likely to dominate over natural convection, which is outside the conditions suitable for simulated microgravity studies. Thus, clinostat motion modes at frame speeds of 80–120 deg s^{-1} are not recommended.

The 0 g and 0.4 g motion modes, on the other hand, indicated laminar flow in the continuous phase and Stokes flow around the particles. Under these conditions, droplet movement relative to the continuous flow was negligible, while viscous and surfaces forces dominated over natural convection, which in turn dominated over forced convection, which describes a state similar to true microgravity in space. Therefore, 0 g and 0.4 g motion modes are recommended to simulate microgravity or partial gravity.

The presented findings need to be confirmed with experimental studies in the future, as multiple simplifications have been assumed in order to apply the scaling analysis *via* dimensionless numbers. Additionally, it is advised to investigate the clinostat motion mode at lower frame rates ($<$80 deg s^{-1}) as well as alternative motion modes the RPM offers.

Conflicts of interest

There are no conflicts to declare.

Data availability

The supplementary information (SI) provides additional information on experimental setups to simulate microgravity in terrestrial gravity (especially the Random Positioning Machine), for the continuous, microfluidic emulsification (how to determine volumetric flow rates based on the oil phase's density), the full data set characterising the obtained emulsions and for the characterisation of the oil phase (linear regression of experimental data to determine the dynamic viscosity below SOR of 0.5). See DOI: **https://doi.org/10.1039/d5sm00436e**.

The movement recordings for the different motion modes (0 g; 0.4 g; clinostat 80 deg s^{-1}; clinostat 100 deg s^{-1}; clinostat

120 deg s^{-1}) of the random positioning machine is archived and publicly available in the Nottingham research repository (DOI: https://doi.org/10.17639/nott.7406).

Acknowledgements

The scholarship support by the PhD Program of the Nottingham-Adelaide Alliance was acknowledged. The Waite Research Institute and the SET Faculty (Science, Engineering, and Technology, formerly known as ECMS), both from the University of Adelaide, have jointly purchased the Random Positioning Machine 2.0 from Airbus. Prof. Volker Hessel and Prof. Ian Fisk acknowledge the support of the Australian Research Council Centre of Excellence 'Plants for Space' [CE230100015]. Prof. Ian Fisk acknowledges funding from Biotechnology and Biological Sciences Research Council [BB/V018108/1].

References

1 M. Dhaval, P. Vaghela, K. Patel, K. Sojitra, M. Patel, S. Patel, K. Dudhat, S. Shah, R. Manek and R. Parmar, *Drug Delivery Transl. Res.*, 2022, **12**(7), 1616–16399.
2 N. Chiu, L. Hewson, I. Fisk and B. Wolf, *Food Funct.*, 2015, **6**, 1428–1434.
3 N. Chiu, A. Tarrega, C. Parmenter, L. Hewson, B. Wolf and I. D. Fisk, *Food Hydrocolloids*, 2017, **69**, 450–458.
4 C. Tan and D. J. McClements, *Foods*, 2021, **10**(4), 812, DOI: 10.3390/foods10040812.
5 D. Venkataramani, A. Tsulaia and S. Amin, *Adv. Colloid Interface Sci.*, 2020, **283**, 102234.
6 P. A. Lovell and F. J. Schork, *Biomacromolecules*, 2020, **21**, 4396–4441.
7 A. Makaya, L. Pambaguian, T. Ghidini, T. Rohr, U. Lafont and A. Meurisse, *CEAS Space J.*, 2023, **15**, 69–75.
8 R. Snyderman, *Biotechnol. J.*, 2012, **7**, 973–979.
9 S. Schmidt, A. T. Nguyen, H. Q. Vu, N. N. Tran, M. Sareela, I. Fisk and V. Hessel, *Adv. Healthcare Mater.*, 2023, **12**(23), 2203363.
10 F. Ravera, K. Dziza, E. Santini, L. Cristofolini and L. Liggieri, *Adv. Colloid Interface Sci.*, 2021, **288**, 102344.
11 A. Drelich, C. Dalmazzone, I. Pezron, L. Liggieri and D. Clausse, *Oil Gas Sci. Technol.*, 2018, **73**, 16.
12 European Space Agency, The ZARM drop tower in Bremen, https://www.esa.int/Education/Drop_Your_Thesis/The_ZARM_drop_tower_in_Bremen, (accessed 2 September 2025).
13 S. M. Kim, H. Kim, D. Yang, J. Park, R. Park, S. Namkoong, J. I. Lee, I. Choi, H. S. Kim, H. Kim and J. Park, *Microgravity Sci. Technol.*, 2017, **29**, 97–106.
14 J. J. W. A. van Loon, *Adv. Space Res.*, 2007, **39**, 1161–1165.
15 S. L. Wuest, S. Richard, S. Kopp, D. Grimm and M. Egli, *BioMed Res. Int.*, 2015, 971474.
16 European Space Agency, Random Positioning Machine, https://www.esa.int/ESA_Multimedia/Videos/2019/04/Random_Positioning_Machine, (accessed 1 October 2025).
17 Yuri, RPM & Clinostat: Simulate Microgravity with Yuri, https://yurigravity.com/platform, (accessed 12 June 2025).
18 Equiprobe, Exploring Microgravity on Earth: The Equiprobe Random Positioning Machine, https://equiprobe.com/rpm/, (accessed 1 October 2025).
19 M. Calvaruso, C. Militello, L. Minafra, V. La Regina, F. Torrisi, G. Pucci, F. P. Cammarata, V. Bravatà, G. I. Forte and G. Russo, *Life*, 2021, **11**(11), 1190.
20 D. Dantuma, R. Elmaddawi, Y. Pathak, A. Grenha, R. De Oliveira, C. Paludo, M. A. Dos Santos and M. A. Dos, *Am. J. Med. Biol. Res.*, 2015, **3**, 102–106.
21 J. L. Clary, C. S. France, K. Lind, R. Shi, J. S. Alexander, J. T. Richards, R. S. Scott, J. Wang, X.-H. Lu and L. Harrison, *Front. Space Technol.*, 2022, **3**, DOI: 10.3389/frspt.2022.1032610.
22 D. Kim, Q. T. T. Nguyen, S. Lee, K. M. Choi, E. J. Lee and J. Y. Park, *npj Microgravity*, 2023, **9**, 63.
23 I. Cariati, R. Bonanni, M. Scimeca, A. M. Rinaldi, M. Marini, U. Tarantino and V. Tancredi, *Life*, 2022, **12**(5), 610.
24 I. Cariati, M. Scimeca, R. Bonanni, R. Triolo, V. Naldi, G. Toro, M. Marini, V. Tancredi, R. Iundusi, E. Gasbarra and U. Tarantino, *Front. Physiol.*, 2022, **13**, DOI: 10.3389/fphys.2022.782000.
25 I. Cariati, R. Bonanni, A. M. Rinaldi, M. Marini, R. Iundusi, E. Gasbarra, V. Tancredi and U. Tarantino, *Front. Physiol.*, 2023, **14**, DOI: 10.3389/fphys.2023.1107933.
26 U. N. Ngwoke, M. C. Ogwu, G. O. Omoregie, P. K. Akpeh and B. Ikhajiagbe, *Plant Growth Regul.*, 2023, **99**, 597–608.
27 S. Alikhani, F. Ghanati, N. Karami, Z. Hajebrahimi, M. Soleimani and M. Alipour, *Plant Cell, Tissue Organ Cult.*, 2024, **158**, 39.
28 B. Chen, A. Zhang, Q. Lu, T. Kuang, C. Lu and X. Wen, *Photosynth. Res.*, 2013, **116**, 93–105.
29 P. Born, M. Braibanti, L. Cristofolini, S. Cohen-Addad, D. J. Durian, S. U. Egelhaaf, M. A. Escobedo-Sánchez, R. Höhler, T. D. Karapantsios, D. Langevin, L. Liggieri, M. Pasquet, E. Rio, A. Salonen, M. Schröter, M. Sperl, R. Sütterlin and A. B. Zuccolotto-Bernez, *Rev. Sci. Instrum.*, 2021, **92**(12), 124503.
30 G. Volpe, C. Bechinger, F. Cichos, R. Golestanian, H. Löwen, M. Sperl and G. Volpe, *npj Microgravity*, 2022, **8**, 54.
31 C. A. D. Leguy, R. Delfos, M. J. B. M. Pourquie, C. Poelma, J. Westerweel and J. J. W. A. van Loon, *Adv. Space Res.*, 2017, **59**, 3045–3057.
32 S. L. Wuest, P. Stern, E. Casartelli and M. Egli, *PLoS One*, 2017, **12**(1), e0170826.
33 A. Gupta, H. B. Eral, T. A. Hatton and P. S. Doyle, *Soft Matter*, 2016, **12**, 1452–1458.
34 Airbus Defense and Space Netherlands B.V., RPM 2.0 User Manual, 2020.
35 R. H. Huijser, *Desktop RPM: New small size microgravity simulator for the bioscience laboratory*, 2000.
36 N. Anarjan and C. P. Tan, *Molecules*, 2013, **18**, 768–777.
37 N. Anton and T. F. Vandamme, *Int. J. Pharm.*, 2009, **377**, 142–147.
38 D. T. Piorkowski and D. J. McClements, *Food Hydrocolloids*, 2014, **42**, 5–41.
39 C. W. Pouton and C. J. H. Porter, *Adv. Drug Delivery Rev.*, 2008, **60**, 625–637.

40 J. Komaiko and D. J. McClements, *J. Food Eng.*, 2015, **146**, 122–128.
41 M. D. Tarn and N. Pamme, *Reference Module in Chemistry, Molecular Sciences and Chemical Engineering*, Elsevier, 2014.
42 J. Cottet and P. Renaud, *Drug Delivery Devices and Therapeutic Systems*, Elsevier, 2020, pp. 3–17.
43 K. Jähnisch, V. Hessel, H. Löwe and M. Baerns, *Angew. Chem., Int. Ed.*, 2004, **43**, 406–446.
44 Vials Direct, MCT Oil Product Information, **https://www.vialsdirect.com.au/product/sterile-usp-pharmaceutical-grade-mct-oil-ultra-filtered-100-purity/**, (accessed 23 July 2025).
45 G. L. Douglas, S. R. Zwart and S. M. Smith, *J. Nutr.*, 2020, **150**, 2242–2244.
46 M. Kraume, *Transportvorgaenge in der Verfahrenstechnik – Grundlagen und apparative Umsetzungen*, Springer, Heidelberg, 2nd edn, 2012.
47 C. G. Stokes, *Trans. Cambridge Philos. Soc.*, 1851, **9**, 8–106.
48 J. Hadamard, *C. R. Acad. Sci.*, 1911, **152**, 1735–1743.
49 W. Rybczynski, *Bull. Int. Acad. Sci. Cracovie*, 1911, **A**, 40–46.
50 S. R. Reddy and H. S. Fogler, *J. Colloid Interface Sci.*, 1981, **82**(1), 128–135.

